UNIVERSITATEA
DIN BUCUREȘTI
VIRTUTE ET SAPIENTIA

FACULTATEA DE CHIMIE

DISERTATION THESIS

Student: BADEA MARA-ALEXANDRA

Supervisor: Prof. Dr. Habil. SIMONA MARGARETA COMAN

2022

Sesiunea IUNIE - IULIE 2022

UNIVERSITATEA DIN BUCUREȘTI

VIRTUTE ET SAPIENTIA

FACULTATEA DE CHIMIE

DECLARAȚIE

Subsemnata Badea Mara-Alexandra, candidat la examenul de Disertație, la Facultatea de Chimie, specializarea Chimia Materialelor Avansate – cu predare în limba engleză declar pe proprie răspundere că lucrarea cu titlul Catalytic synthesis of alanine by lactic acid amination, având drept coordonator pe Prof. Dr. Habil. Simona-Margareta Coman depusă în vederea susținerii publice reprezintă rezultatul muncii mele, are la bază rezultate experimentale obținute de mine și informații obținute din surse care au fost citate și indicate, conform normelor etice în note de subsol și bibliografie. Declar că nu am folosit în mod tacit sau ilegal munca altora și nici o parte a lucrării nu încalcă drepturile de proprietate intelectuală ale altcuiva, persoană fizică sau juridică. Declar de asemenea că lucrarea nu a mai fost prezentată în această formă vreunei instituții de învățământ superior în vederea obținerii unui grad / titlul științific sau didactic.

Dată: 27.06.2022

Semnătură candidat

M. Badea

Coordonator: Prof. Dr. Habil. Simona-Margareta Coman

Semnătură:

FACULTATEA DE CHIMIE

APROBAT

Director departament:

Conf. Dr. Habil. Ileana Fărcășanu

Ileana Farcasanu

CERERE pentru susținerea Lucrării de Disertație

„Catalytic Synthesis of Alanine by Lactic Acid Amination"

Subsemnata, Badea Mara-Alexandra, absolventă a Facultății de Chimie, la masterul „Chemistry of Advanced Materials", vă rog să aprobați susținerea publică a lucrării mele de dizertație, cu titlul "Catalytic Synthesis of Alanine by Lactic Acid Amination", în sesiunea Iunie-Iulie, 2022, coordonatorul lucrării fiind Prof. Dr. Habil. Simona-Margareta Coman.

Conținutul lucrării:
1. Partea de literatură *(tematica urmărită, obiectivele referatului de literatură)*
S-a realizat o cercetare exhaustivă a literaturii disponibile privind utilizarea biomasei pentru sinteze de chimicale fine sau molecule platformă care, mai departe, pot fi convertite în produse cu valoare adăugată pe piața de desfacere. Totodată, s-a realizat o amplă documentare pe problematica design-ului catalizatorilor utilizați în astfel de procese și pe sinteza de aminoacizi. Importanța aminoacizilor derivă din faptul ca sunt elementele de bază ale biosintezei proteinelor și sunt utilizați în nenumărate aplicații industriale, inclusiv în produsele alimentare umane, în hrana animalelor și ca precursori pentru materiale bio-plastice. Ca atare, dezvoltarea unor metode chimice eficiente de transformare a materiilor prime abundente și regenerabile în aminoacizi este extrem de importantă dar puținele încercări raportate în literatură arată insuccesul relativ al acestora. Ca alternativă, abordările chemo-catalitice pentru producerea de aminoacizi din materii prime regenerabile, cum ar fi zaharurile, ar putea oferi un mijloc rapid și potențial mai eficient de sinteză al acestora. Din păcate însă, o abordare durabilă și generalizabilă a utilizării NH3 pentru sinteza directă a aminoacizilor din materii prime abundente și regenerabile rămâne o raritate. Una dintre cele mai studiate astfel de abordări este sinteza alaninei prin aminarea acidului lactic, în prezența catalizatorilor pe bază de ruteniu depus pe suporturi nanotuburi de carbon, nanotuburi de carbon dopate cu azot sau dioxid de titan. În ciuda acestor progrese însă, producția chimică de alanină din resurse regenerabile rămâne la început.

2. Partea originală *(contribuții metodice, didactice, utilizarea unor programe de calcul, realizarea unor noi programe de calcul, realizarea și testarea unei instalații noi, determinări experimentale proprii, dezvoltare/validare metode, modelarea unor procese fizico-chimice, prelucrarea și interpretarea rezultatelor, etc.)*
Partea experimentală a lucrării este structurată în doua capitole. Primul capitol conține descrierea metodologiilor de sinteză ale catalizatorilor, tehnicile de caracterizare utilizate, condițiile de testare ale acestora în aminarea acidului lactic și metoda de analiza a produșilor de reacție obținuți. În al doilea capitol sunt discutate pe larg rezultatele obținute încercându-se o corelare a proprietăților catalitice cu performanțele acestora în aplicația catalitică. Pentru catalizatorii studiați, pe bază de ruteniu, s-au utilizat trei tipuri diferite de suporturi: nanotuburi de carbon, nanotuburi de carbon

oxidate și particule magnetice acoperite cu silice și APTES. Prepararea celor trei catalizatori a presupus impregnarea acestora cu 1%, 3% și 5wt% ruteniu, urmată de calcinare și reducere. Catalizatorii au fost caracterizați utilizând tehnici precum difracție de raze X (XRD), adsorbție-desorbție de azot lichid la -196°C, desorbție la temperatură programată de H_2 și NH_3 (H_2-TPD, NH_3-TPD), spectroscopie Raman și IR, analiză termogravimetrică (TG) și microscopie electronică de scanning cuplată cu cea de transmisie (STEM). Prelucrarea datelor s-a realizat utilizând softul Origin. Testele catalitice au fost realizate în autoclavă, sub presiune de hidrogen. Amestecurile de reacție au fost apoi aduse la sec, silanizate și analizate cu ajutorul unui gas cromatograf cuplat cu spectrometrie de masă (GC-MS). Rezultatele catalice au fost prelucrate utilizând softul Excel.

Aprecierea coordonatorului:

Activitatea pe care studenta Mara-Alexandra BADEA a depus-o a condus la o lucrare de disertație structurată în trei capitole (aspecte teoretice, metodologii experimentale și rezultate și discuții) la care se adaugă secțiunile de concluzii, diseminare și referințe bibliografice. În toată această perioadă Mara a dat dovadă de o dorință remarcabilă de progres științific reușind într-un timp relativ scurt să dobândească cunoștințe importante atât în sinteza de materiale catalitice cât și în utilizarea metodelor de investigație ale acestora. Deși munca susținută și relativ neîntreruptă nu a fost lipsită de anumite întârzieri obiective, tenacitatea și dorința de progres manifestată de Mara în această perioadă au asigurat încheierea cu succes a acestei etape profesionale.

Implicarea candidatei în realizarea studiului de literatură și a etapelor de cercetare experimentală au generat un volum extrem de mare de informații utile noi, care fac obiectul acestei Lucrări de Disertație. Ca atare, sunt extrem de mulțumită de tenacitatea și efortul susținut de studenta Mara-Alexandra BADEA în realizarea acestei teze de disertație. Apreciez, de asemenea, că Mara, datorită adaptabilității rapide la diferite situații particulare care solicită o implicare pe măsură, dispune de un potențial foarte mare în dezvoltarea unei activități de cercetare similare viitoare.

Rezultatele obținute în această Lucrare de Disertație fac obiectul unei comunicări științifice (Poster), cu titlul „Catalytic production of amino acids from biomass-derived intermediates", autori: M.-A. Badea, B. Cojocaru, V. I. Parvulescu, S. M. Coman, prezentată de către candidată la Simpozionul „The 13th International Symposium of the Romanian Catalysis Society (RomCat2022), 22-24 Iunie 2022, Băile Govora, România, organizat de Societatea de Cataliză din România, în parteneriat cu Universitatea din București și Institutul Național de Cercetare și Dezvoltare pentru Tehnologii Criogenice și Izotopice (ICSI).

Acordul conducătorului pentru susținerea lucrării: Da

Coordonator: Prof. Dr. Habil. Simona-Margareta Coman

Semnătură:

Data completării cererii: 27.06.2022

FACULTY OF CHEMISTRY
DEPARTMENT OF ORGANIC CHEMISTRY, BIOCHEMISTRY AND CATALYSIS

MSc Thesis

Catalytic synthesis of alanine by lactic acid amination

MASTER: CHEMISTRY OF ADVANCED MATERIALS

STUDENT: MARA ALEXANDRA BADEA

SCIENTIFIC COORDINATOR:

Prof. Dr. Simona-Margareta Coman

July 1, 2022

CONTENT

Introduction

Due to their versatility amino acids are valuable products for industry [1]. Amino acids are primarily manufactured *via* microbial cultivation processes, which are costly, time consuming, and require extensive separations processes. The development of efficient chemical methods to convert abundant and renewable feedstocks into amino acids is, therefore, highly attractive but it have been largely unsuccessful to date. As an alternative, chemocatalytic approaches could offer a rapid and potentially more efficient means of amino acid synthesis, but efforts to date have been limited by the development of facile chemistry and associated catalyst materials to selectively produce α-amino acids.

In our knowledge, only one recent report on the directly catalytic transformation of the lignocellulosic biomass-derived α-hydroxyl acids into α-amino acids, including alanine, leucine, valine, aspartic acid, and phenylalanine in high yields exist in literature [2]. The synthesis follows a dehydrogenation-reductive amination pathway, with dehydrogenation as the rate-determining step. Ruthenium nanoparticles supported on carbon nanotubes (Ru/CNT) exhibit exceptional catalytic efficiency due to the unique, reversible enhancement effect of NH_3 on Ru in dehydrogenation step.

The CNT application in heterogeneous catalysis is based on their specific important characteristics such as: (i) resistance to acid/basic media, (ii) possibility to control, up to certain limits, the porosity and surface chemistry and (iii) easy recovery of precious metals by support burning resulting in a low environmental impact [3]. The combination of these properties makes CNT attractive and competitive catalyst supports by comparison with activated carbons.

In the case of as-produced CNT's it has to be noticed that such materials do not possess a high amount of functional groups on their surface and mainly surface defects can be considered as anchoring sites for metals. In order to evaluate the role of surface defects on the final metal dispersion, the interaction between iron, cobalt or nickel and MWNT, SWNT, activated carbon or layered graphite has been studied [4]. On SWNT and layered graphite, no coating was observed due to the low density of surface defects. However, for MWNT and activated carbon, a better wetting has been achieved and, in the case of iron on MWNT, a particle size of 5–15 nm has been measured. Several other metals were deposited on MWNT by using the wetness impregnation technique. For instance, palladium, platinum, gold and silver particles obtained presented a mean size of 7, 8, 8 and 17 nm, respectively, and were mostly found on the outer surface of the CNT [5].

Like for classical carbon materials used in catalysis the possibility of chemical or thermal activation, in order to modify the nature and concentration of surface functional groups, has been studied in the case of CNT. Among the different techniques that have been applied for the more or less

pronounced surface oxidation, nitric acid treatments are the most common and it has been shown that surface oxygen functionalities like carboxylic groups can be introduced on the outer and possibly inner walls of the CNT [6]. In the case of MWNT the main significant structural modification occurs on the nanotubes tip and can result(s) in their opening. The formation of edges and steps on the graphene sheets is also possible [7]. Deposition of different metals (i.e., silver, cobalt, cerium) on nitric-acid treated MWNT showed the critical factor to well dispersed nanoparticles is the oxidation step [3].

On the other hand, magnetic nanoparticles (MNPs) have been gaining increasing interest in the last years due to their valuable properties such as high surface area, low toxicity and super-paramagnetic behavior [8]. This intrinsic property may allow an easier separation from reaction mixtures by the use of an external magnetic field. In addition, the presence of a large number of hydroxyl groups on the external surface affords both the deposition of inorganic shells containing different catalytic active phases and the direct immobilization of a variety of catalytic functionalities *via* covalent bonds [9]. In this context, not long ago an efficient $Ru(4wt\%)@MNP\text{-}SiO_2$ catalyst for the oxidation of levulinic acid (LA) to succinic acid (SA) (S_{SA} = 96-98% for X_{LA} = 59-79%) was reported [10].

1. Theoretical aspects

Due to the rapid population growth and vast economic developments nowadays there is an increase in global energy demand that is estimated to double between 2000 and 2035 [11]. Fossil fuel sources, such as crude oil, coal and natural gas currently hold the major share of energy supply. However, these sources are non-renewable and global petroleum production is predicted to peak by 2020 due to increasing demand for chemical industries, before decaying.

Another major concern of the 21st century is the increasing levels of greenhouse emissions (CO_2 in special) caused by the enormous consumption of fossil fuels. The global CO_2 emissions reached an all-time record of 41.5 ± 4.4 billion tonnes in 2017, contributing to an atmospheric CO_2 concentration of 408 ppm, the highest since the beginning of the industrial revolution. If this situation continues, global average temperatures are estimated to increase drastically in the range of $2.5 - 5.4$ °C [11]. In the same manner, global warming is a major threat to humankind as well as to the biosphere if we think at the increased rate and intensity of many climate catastrophes from recent time. Due to this situation created worldwide the scientists from many countries try to find alternative pathways to replace the actual industry which is based almost in totally on petroleum with an industry based on clean, sustainable resources for the production of fuels and chemicals.

Various renewable resources are available for the production of energy and/or chemicals. Some of these resources are: wind, geothermal, solar, hydropower and biomass. Although renewable energy from wind and water holds considerable potential, it is insufficient and incapable to fill the entire global energy demand. For a short and medium term solution to the deficit of both sustainable energy and renewable carbon, most experts look to biomass as a most viable alternative source. As a highly abundant natural carbon source, biomass is considered a promising renewable alternative to fossil fuels that can be transformed into a wide range of value-added chemicals, clean solvents and biodiesel. Several biomass resources such as animal waste, agricultural crops, wood and aquatic plants are available for the production of sustainable chemicals. If we think at the fuels, which are of great necessity in our society, we realize that the humankind is on the verge of collapse. Bearing this in mind, we need to give it a chance to the biofuels with products derived from lignocellulosic biomass, because this is the future.

Lignocellulosic biomass is the most abundant and bio-renewable resource, with great potential for sustainable production of chemicals and fuels [12]. Lignocellulose functions as the most important structural component in a majority of plants, making it widely available in much larger quantities than starch, oils and fats, the source materials of first generation biofuels [13]. Any materials rich in cellulose, hemicellulose and lignin are commonly referred to as lignocellulosic biomass. For example, wood, bamboo, grass and their derived pulp and paper, and agricultural residues like corn cobs and sugarcane bagasse are typical sources of lignocellulosic biomass. Generally, most of the lignocellulosic biomass contains 35-50% cellulose, 20-35% hemicellulose and 10-25% lignin. Unfortunately, these components are indigestible by humans, but are readily available in several industrial waste streams, especially from the paper and agricultural industries. This severs to the direct competition between lignocellulose valorization and human food supply.

Since cellulose is the main component of lignocellulosic biomass it is imperative to know more about it. Cellulose is one of the most abundant compounds on earth because it is contained in almost all woody materials. It has the same molecular formula as amylose, one of the main components of starch ($C_6H_{10}O_5$), but between them is a fundamental difference: in amylose the glucose monomers are linked by α-1,4-glycosidic bonds whereas in cellulose the glucose monomers are linked by β-1,4-glycosidic bonds as shown in Figure 1. This seemingly trivial difference has important physico-chemical consequences.
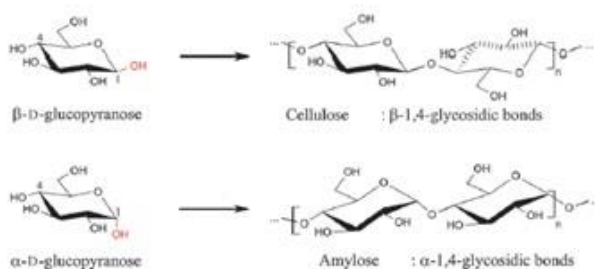
Figure 1. Structure of cellulose and amylose (starch) [13]

In cellulose, the glucose monomers are forced into a $^4C_1$ chair conformation, while successive monomers are rotated over 180° around the polymer axis, to satisfy the bond angle of the bridging oxygen. This forces the hydroxyl and hydroxymethyl groups in an equatorial position, stabilizing the chair conformation and decreasing the flexibility of the glycosidic bond. As a result, the cellulose chain is linear, forming a rigid polymer, whereas amylose chains show more flexibility. Two intramolecular hydrogen bonds per anhydroglucopyranose unit further increase its rigidity. Every cellulose crystal phase exhibits a O3-H-O5ʹ bond. In addition, another crystal phase dependent hydrogen bond is formed. Finally, the β bond is intrinsically more stable than the α bond, presented in amylose.

The main utilization of cellulose in industry is currently limited to textiles and paper manufacturing. In some biological processes such as fermentation and enzymatic catalysis, peculiar enzymes, bacteria and other microorganisms are used to break down cellulose molecules and thus a few commodity chemicals can be obtained. Nevertheless, such biological processes generally suffer from unsolvable problems such as low efficiencies, narrow reaction conditions and limited scale of production. Chemo-catalytic conversion of cellulose [12] has been around for some time, but it only receives serious attention with the advent of a series of novel chemo-catalytic reaction routes since the fossil oil crisis in the 1970s. Nowadays, researchers in the entire world try to find ways to break down more easily cellulose and transform it in useful chemicals. Some typical chemicals and fuels which can be produced by chemo-catalytic conversion of cellulose by different chemical processes as presented in the Scheme 1.

Clearly, a variety of fuels, including ethanol, hydrogen, methane and chemicals such as glucose, fructose, sorbitol, levulinic acid and lactic acid can be obtained from catalytic conversion of lignocellulosic biomass. Lignocellulosic biomass can also be used to produce syngas ($CO + H_2$) which can then be transformed into fuels and myriad chemicals. In many instances, depolymerization and hydrolysis of cellulose to glucose monomer is regarded a necessary first step. Then glucose is further catalytically degraded into various intermediates, chemicals and fuels, following the A route.

4

Following the route B, it is desirable to obtain fine chemicals directly from cellulose, without having one more step implying the formation of glucose.
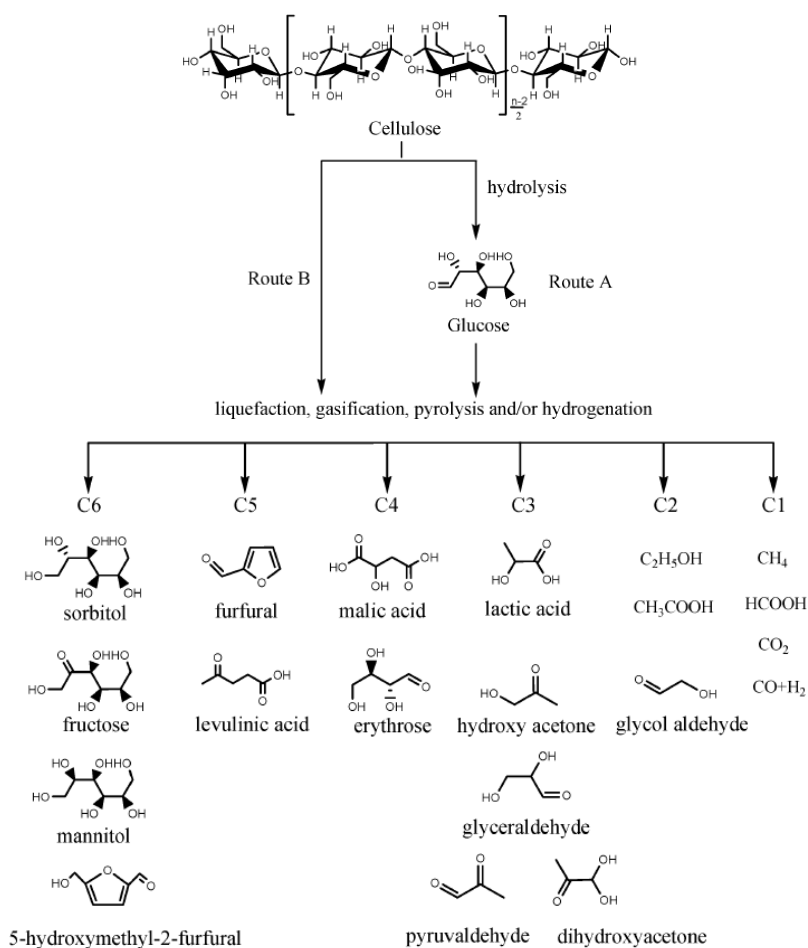
Scheme 1. Potential chemicals and fuels from the catalytic conversion of cellulose

Compared to cellulose, hemicellulose has a very diverse composition [13] containing several pentoses (mostly xylose and arabinose), hexoses (mostly galactose, glucose and manose) and nonsugar compounds as monomers. Furthermore, a typical hemicellulose chain is branched and shorter than that in cellulose, inhibiting crystal formation and making hemicellulose much easier to hydrolyse than cellulose. The utilization of the saccharides derived from hemicellulose is essential for its efficient transformation to biofuels (mainly ethanol) or other high value-added chemicals. These two alternative purposes for hemicellulose valorization can be attained by chemical or biological conversion of the hemicellulosic monomers. Hemicellulose can be depolymerized into monomeric and oligomeric components with high purity and yield by chemical, enzymatic or thermal processes [14].

Lignin is another major component of lignocellulose, mainly present in woody biomass. It is a heavily branched and interconnected hydrophobic polymer consisting of three typical aromatic monomers: p-coumaryl alcohol, coniferyl alcohol and sinapyl alcohol. These alcohols polymerize by random coupling reactions, forming a very complex structure. Lignin is extremely resistant to degradation. The reactivity of lignins is dominated by the substructures containing aryl esthers, biaryls, phenols, benzyl and aliphatic alcohols.

Related to the activities connected to the biomass conversion, the biorefining concept was introduced not long ago and defined as a "facility that integrates biomass conversion processes and equipment to produce fuels, power and chemicals from biomass" [15]. In principle, the biorefining concept is similar with today's petroleum refineries, the difference being the feedstocks. Regarding the polymeric components of lignocellulose, almost each carbon atom is connected to an oxygen atom. Because of this, in biorefineries, is necessary a controlled defunctionalization (e.g. reducing the oxygen content through efficient catalytic processes) rather than the functionalization used in the chemical industry so far. Unfortunately, this means that most of the developed processes in the petrochemical and chemical industry are not suitable for converting biomass, and alternative pathways for the production of fuels and chemicals should be developed. Moreover, for sustainable development and environmental protection reasons, an efficient biorefinery unit should provide a complete valorization of the biomass source, by performing the overall processes with a minimum loss of energy and mass, and should maximize the overall value of the production chain with the minimum formation of wastes.

Solid catalysts are in principle very suitable for the processing of biomass. However, the requirements for biomass conversion are rather different, compared to the processing of hydrocarbon feedstocks, which form the backbone of our current energy and raw materials supply. A large number of technologies based on biological, thermal, and chemical processes have been developed for biomass valorization. Among those, chemical processing of biomass is of paramount research interest as the resulting products can exhibit relatively equating characteristics to petro-based products [11]. Various kinds of chemical processes, such as fast pyrolysis, hydro-processing, oxidation, dehydration, hydrolysis, transesterification, isomerisation, and many others have been reported, in which the application of a catalyst is crucial to enhance reaction rates and to obtain high yields of desirable products in a short time period. Indeed, catalysis is a key technology in modern chemical industry and plays an essential role in the production of a vast majority of bulk and commodity chemicals. Catalysis greatly contributes to the development of new, greener, and potential chemical processes, offering

feasible alternatives to stoichiometric reactions, thus acting as a driving force towards a more sustainable chemical industry.

Homogeneous and heterogeneous catalysts are both used in petrochemical industry [11] as well as in biomass upgrading. Homogeneous catalysts, where the active sites are in the same phase as the reactants, can interact efficiently with the reaction substrates, typically resulting in higher turnover frequency (TOF) rates compared to heterogeneous catalysts. However, homogeneous catalysts are often associated with high toxicity, corrosivity, energy-intensive separation and purification procedures, and inefficient reusability. Stringent government regulations have therefore directed chemical industries to search for alternative catalytic materials. In this respect, heterogeneous catalysis, where the catalyst exists in a different phase (typically solids) as the reactants (mostly liquids or gasses), could offer tremendous potentials for several energy and environmental-related applications including biomass upgrading. Availability of facile preparation methods, low production costs, remarkable robustness, high resistance to common reaction conditions (moisture, air, pressure, and temperature) and durable lifetime are some of the primary advantages of solid catalysts. More importantly, solid catalysts can be efficiently recovered from reaction mixtures and can be readily reused in multiple catalytic cycles, making the process cost-effective and more sustainable. Separation processes represent more than half of the total investment in equipment for the chemical and fuel industries [16]. It is not overstatement that the separation costs are a decisive factor in the final analysis of a new process. So, the ease of separation of solid catalysts can be a crucial advantage. However, it is necessary that these catalysts have high selectivities in order to guarantee the cost-effectiveness of the process.

If we talk about the usage of solid catalysts (heterogeneous catalysis) we need to bear in mind that are quite a few challenges face ahead in the design of these. Some of these challenges are: the discovery of new reaction media, the optimum catalyst composition, the porosity of the catalyst and the active sites presented by last. Carbon materials have emerged as promising catalyst supports as well as metal-free active phase catalysts for various biomass transformation reactions [11]. They exhibit a broad spectrum of crucial catalytic properties such as large specific surface area, tailorable porous structures and surface chemistry, excellent chemical stability in acid or base media, remarkable hydrothermal stability, and efficient functionalisation. Many types of conventional carbon materials, such as activated carbon, carbon black, glassy carbon, pyrolytic carbon, and polymer-derived carbon have been employed for stabilizing catalytic active phases. Owing to high specific surface area and rich surface chemistry, these carbon materials allow the formation of highly dispersed metal particles (Pd,

Ru, Ni, Cu, Ag, Fe, etc.) throughout the catalyst matrix, resulting in enhanced resistance to sintering even at higher metal loadings and elevated temperature conditions. Moreover, advances in materials science and nanotechnology have provided several innovative strategies for the development of new carbon materials, such as carbon nanotubes (CNTs), graphene, and mesoporous carbons that can be used as catalyst supports or active catalysts.

Carbon nanotubes (CNTs) are characterized by a hexagonal arrangement of sp^2 carbons with well-controlled cavity geometries. CNTs can be classified as single-walled (SWCNTs) and multi-walled CNTs (MWCNTs) based on the number of carbon layers present in the tubular wall. SWCNTs are semiconductive with diameters of around 0.4–2 nm, whereas MWCNTs are metallic. Interestingly, the cavities of CNTs can prevent the aggregation of active metal nanoparticles (NPs) during catalyst synthesis or catalytic reactions. Defect sites and surface chemistry are the key parameters that determine the catalytic efficiency of carbon materials in biomass conversions. For example, defect sites incorporated into the sp^2 framework of CNTs, graphene or activated carbon can strongly influence surface properties and catalytic functionalities. Heteroatom doping is an appealing strategy, which exploits defect structures in carbon materials. Carbon nanotubes offer potential possibilities for stabilising metal NPs, metal oxides, acid–base functional molecules, and even complex hierarchical hybrids. CNTs exhibit defective sp^2 carbon surfaces and improved electron transport, which facilitates the interaction of active phases with the CNTs. In addition to preventing particle aggregation, the nanoscale confinement within CNTs can also control the diffusion of reactive species and their interactions with the active phases. These fascinating characteristics have been exploited in the field of biomass upgrading, in order to achieve improved conversion rates with high yields of desired products.

A prime objective in the catalytic conversion of lignocellulosic feedstocks is the improving of the catalysts efficiency and selectivity towards value-added products. However, the incorporation of compatible catalytic processes in the actual infrastructure of petrochemical industry plants requires biomass feedstocks to be converted into building block chemicals with fewer oxygenated groups. These building block chemicals, also known as "platform molecules", are molecules with multiple functional groups that possess the potential to be transformed into new families of useful chemicals. The most important 12 platform molecules [17] that can be produced from sugars via biological or chemical conversions and can subsequently be converted to a number of high-value bio-based chemicals or materials are given in the Figure 2.
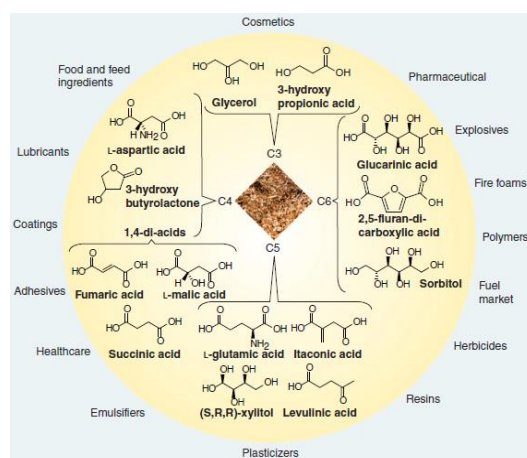
Figure 2. The 12 building blocks (platform molecules) identified in the biomass feedstock conversion [17]

Lactic acid (2-hydroxypropanoic acid, LA) is an encouraging renewable building block for the development of biodegradable plastics and to substitute current petrochemical-based materials [18] but it is also extensively employed in the food and pharmaceutical industries. New applications [19] have been recently intensified in the field of commodity chemicals such as propylene oxide and propanoic acid, liquid fuels and polymers. In Scheme 2 it can be seen some chemicals obtained starting from lactic acid as well as the specific routes [20].
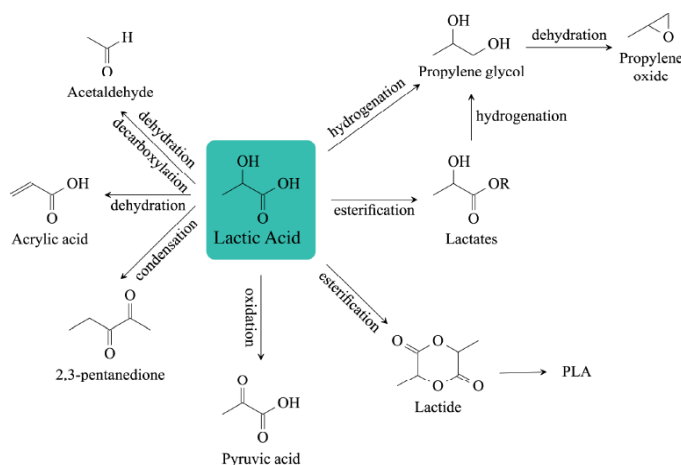
Scheme 2. Lactic acid as a platform chemical [20]

LA and other hydroxy acids can also be used as raw materials in the catalytic synthesis of the amino acids, which are the building blocks of proteins and the primary source of nitrogen for tissues in the human body. Nowadays, amino acids are widely produced and used in many fields, their annual production reaching about 6.5 million tons in 2014 [1].
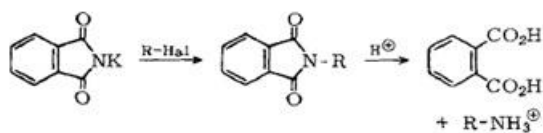
The literature for the use and transformation of amino acids is extremely diverse. In general, however, these focus on the use of amino acids in nutrition, medicine, impact on physiological function, along with their use as platform molecules. In particular, they promote health by several actions, including reduction of the adiposity, regulation of the muscle protein metabolism and the control of the growth and immunity of the organism. Also, it is well documented that amino acids deficiency causes serious diseases, both in humans and animals [21]. Therefore, the interest in investigating and developing new routes to produce them in a more cost-effective and sustainable way has significantly increased in the last years.

In present, amino acids are produced through three different routes: microbial processes (fermentation and enzymatic synthesis), chemical synthesis and extraction from protein-hydrolysates. However, most of the current industrial processes for amino acids production are based on fermentation route, under aerobic or anaerobic conditions, and several microorganism are used in order to convert the sugars present in a substrate into a broad spectrum of amino acids [22]. Generally, the fermentation takes place in an aqueous medium containing essential nutrients such as sources of carbon, nitrogen, phosphorus and sulphur, vitamins and minerals. Identifying a suitable carbon source is a major challenge of the process, because it should not only serve as an energy source for the microorganism, but also as a precursor for the structural skeleton of the amino acid metabolite [1].

The second biological process in the production of amino acids is the enzymatic one or the enzymatic conversion and is based on the action of an enzyme or a combination of enzymes to catalyze the production of the desired amino acids [21].

Historically, chemical synthesis has been the classical pathway to produce achiral amino acids like glycine or a racemic mixture of D,L-methionine or D,L-alanine [21]. In present, the chemical synthesis refers to the Strecker synthesis (production of methionine), the Gabriel malonic ester synthesis (when amino acids are obtained as secondary product) and the Miller synthesis (which aims to obtain amino acids by reproducing the primitive conditions when organic compounds were formed in an atmosphere rich in methane, ammonia, water and hydrogen) [23].

The Strecker synthesis was reported for the first time in 1850. According to this reaction the conversion of an aldehyde or ketone and amine or ammonia to α-amino acids can be achieved by means of an acid catalysts, metal cyanide and water, as shows in Scheme 3.

Scheme 3. Strecker synthesis of alanine [24]

The Strecker synthesis of amino acids has been considered as one of the modes of formation of amino acids in the primordial Earth [24]. In particular it consists in the reaction of an aldehyde with hydrogen cyanide and D-α-methylbenzylamine in methanol, followed by the hydrolysis of the resulting amino nitrile to yield the N-α-methylbenzyl amino acid. Finally, a catalytic hydrogenolysis is performed to remove the metylbenzyl group from the amino acid molecule [21]. The main drawbacks of the chemical synthesis are associated to the price of the catalyst as well as to the use of hazardous cyanide sources. To overcome these problems new methods were developed in 1963 by K. Harada [24], starting from the catalytic asymmetric Strecker-type reaction.

The most common industrial chemical process for the manufacture of racemic amino acids is the so-called Bucherer-Bergs method [25] which is a variant for the Strecker synthesis. This method proceeds via a hydantoin intermediate that is generated from an aldehyde, hydrogen cyanide and an ammonium salt. However, the approach is far less attractive than fermentation or enzymatic catalysis because an expensive optical resolution step is required to isolate the bio-active L-isomer from the amino acid racemate [1]. This approach is therefore involved only in the production of achiral glycine and D,L-methionine, since the adults and animals are able to convert D-methionine to the L-isomer by transamination. Although the Bucherer-Bergs approach is the most common because of its simplicity and effectiveness, the main drawbacks of this method are the long reaction time and the elevated temperature.

Another method of producing amino acids is the Gabriel malonic ester synthesis. The reaction takes place in two steps as shown in the Scheme 4.

Scheme 4. Gabriel's synthesis [26]

In the first step potassium phtalimide reacts with halogenoalkanes and with a variety of other alkylating agents and leads to the N-alkylphtalimide. Furhermore, the N-substituted phtalimides may be converted into the corresponding primary amine by hydrolysis or hydrazinolysis [26]. The importance of the Gabriel synthesis lies in the absence of secondary or tertiary amine contamination of the primary amine and the toleration of a very wide range of other functional groups in the molecule. In the same time, the mild conditions are now available for accomplishing both stages so there is hope.

The last production method of amino acids is the Miller`s synthesis which is based on the idea that organic compounds that serve as the basis of life were formed when the earth had an atmosphere of methane, ammonia, water and hydrogen, instead of carbon dioxide, nitrogen, oxygen and water [23]. In order to test this Miller built an apparatus (Figure 3) which circulated CH_4, NH_3, H_2O and H_2, past an electric charge. Electrical discharge, according to Miller, may have played a significant role in the formation of compounds in the primitive atmosphere.
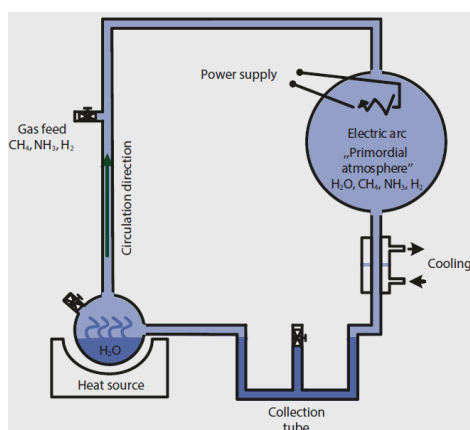
Figure 3. The apparatus used in Miller's synthesis [23]

Water is boiled in the flask and it is mixed with the gases in the 5 liters flask. Then, the water circulates past the electrodes, condenses and empties back into the boiling flask. The U-tube is used because it prevents circulation in the opposite direction. The acids and amino acids formed in the discharge, not being volatile, accumulate in the water phase. In the condensed water phase, various

organic molecules were detected at the end of the experiment, including larger amounts of the amino acids glycine and alanine. It is regarded to be certain that these were formed by Strecker synthesis with the intermediate products hydrocyanic acid, formaldehyde and acetaldehyde, respectively [27].

In present are many attempts to transform lignocellulose biomass-derived α-keto acids and α-hydroxy acids into α-amino acids. In this context W.Deng et al. [2] reported the catalytic synthesis of α-amino acids, including alanine, leucine, valine, aspartic acid and phenylalanine, in high yields, in the presence of ruthenium nanoparticles supported on carbon nanotubes (Ru/CNT). The reaction mechanism is presented in the Scheme 5.
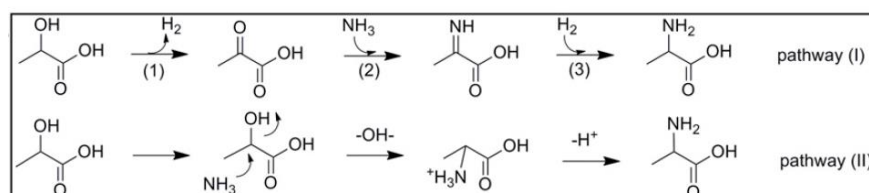
Scheme 5. Two possible reaction pathways for amination of lactic acid to alanine [2]

The catalyst exhibits exceptional efficiency compared with catalysts based on other metals. This happens due to the unique, reversible enhancement effect of NH_3 on Ru in dehydrogenation step. Based on the catalytic system, a two-step chemical process was designed to convert glucose to alanine in 43% yield, comparable with the well-established microbial cultivation process presented above. The presented strategy enables a route for the production of amino acids from renewable feedstocks.

Another pathway of obtaining amino acids (in special alanine) was proposed by Y.Wang et al.[17]. The procedure involves a one-step convertion of the crude glycerol from the biodiesel industry into 43% yield alanine over a Ru_1Ni_7/MgO catalyst. The multifunctional catalytic system promotes glycerol conversion into lactic acid, and then into alanine, as shown in Figure 4.
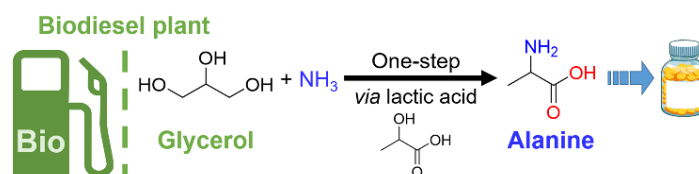

Figure 4. An illustration of one-step conversion of waste glycerol to alanine [16]

They concluded, after performing X-ray absorption spectroscopy and scanning transmission electron microscopy, that existent bimetallic RuNi species and Ni-doped Ru substantially decreases the

E_a of C-H bond dissociation of the lactate alkoxide to form pyruvate, which is the rate determining step. A plausible explanation for this behavior is that the unreacted glycerol inhibits lactic acid and amination reaction.

An attempt of converting biomass to amino acids was made in 2020 by S. Song et al. [28] by using CdS nanosheets, an efficient and stable catalyst which exhibits a higher activity in production of alanine from lactic acid, compared to commercial CdS as well as to CdS nanoobjects bearing other morphologies. The occurring reaction, presented in Figure 5 is a photocatalytic one, CdS representing the only material able to promote the desired transformation under visible light.
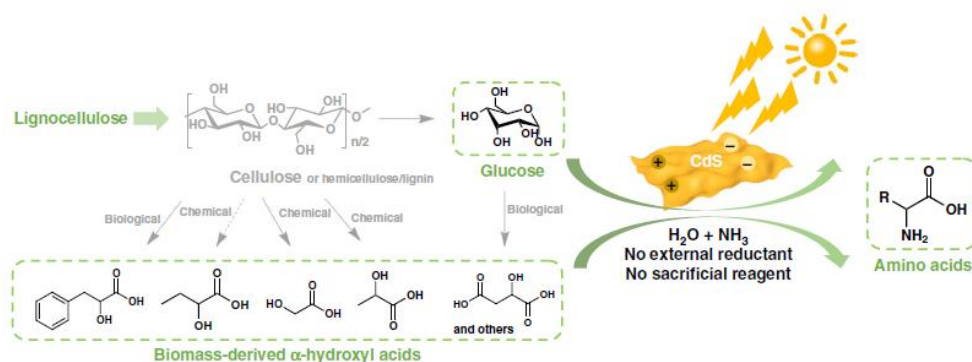
Figure 5. Photocatalytic amination of glucose or biomass-derived α-hydroxyl acids to amino acids [28]

The unique properties of CdS nanosheets are attributed mainly to the preferential formation of oxygen-centered radicals to promote α-hydroxyl acids conversion to α-keto acids and partially to the poor H_2 evolution which is an undesired reaction. Encouragingly, a number of amino acids were prepared using the proposed protocol, with high yields, and one-pot conversion of glucose to alanine was also achieved, under mild conditions.

T.Fukushima and M. Yamauchi [29] made another attempt to transform biomass into amino acids by electrochemical synthesis. They reported that seven amino acids were electrochemically synthesized from biomass-derivable α-keto acids and NH_2OH with faradaic efficiencies (FEs) of 77-99%, using an earth-abundant TiO_2 catalysts.

2. Objectives

The aim of this work was to develop efficient solid catalysts able to directly transform lignocellulosic biomass-derived lactic acid (LA) into alanine (AL) through a dehydrogenation-reductive amination pathway. For this a series of Ru-based catalysts with (1) as-received MWCNT, (2) oxidised MWCNT and (3) magnetic nanoparticles (MNPs) carriers and 1wt%, 3wt% and 5wt%Ru were prepared and characterised.

(1) As already specified, literature indicates that ruthenium nanoparticles supported on carbon nanotubes (Ru/CNT) exhibit exceptional efficiency compared with catalysts based on other metals, due to the unique, reversible enhancement effect of NH_3 on Ru in dehydrogenation step. However, the authors claim the use of a catalyst with only 3wt%Ru, prepared by impregnation on as-received CNT. Much more attention must be paid to the concentration of ruthenium which can lead to ruthenium particles with varying degrees of dispersion and oxidation, these characteristics being able to decisively influence the course of the reaction in which they are applied.

(2) Different oxidation processes were applied in the view of producing functionalized CNTs and their use as carrier for ruthenium deposition, in the next step of the research. By using such type of carriers (i.e., as-received CNT and oxidized CNT) Ru-based catalysts with different catalytic features related to the metal dispersion, location (ruthenium in- and out-tubes) and reduction degree, can be easily created.

(3) To overcome the catalysts separation issue, the use of magnetic nanoparticles emerge as a viable solution; their insoluble and paramagnetic nature enables their easy and efficient separation from the reaction mixture with an external magnet. That is why, a second kind of Ru-based catalysts used as carrier magnetic nanoparticles (MNP) for the synthesis of cationic Ru(III)/functionalized silica coated magnetite nanoparticles.

3. Experimental part

All the chemicals and reagents were of analytical purity grade, purchased from Sigma-Aldrich and used without further purification. Two kind of multi-walled carbon nanotubes (MWCNTs) were purchased with the following features: (1) preparation method Catalytic Chemical Vapor Deposition (CVD) (CoMoCAT®), over 95% carbon, O.D×L/6-9 nm × 5 μm and armchair configuration, and (2) preparation method Catalytic Chemical Vapor Deposition, over 90% carbon basis, D×L/110-170 nm ×

5-9 μm and armchair configuration. Hydrated ruthenium chloride (RuCl$_3$xH$_2$O) had ~37% Ru basis. PTFE membrane filters with 0.45 μm pore size were purchased from Merck.

3.1. Materials preparation methodologies

3.1.1. Ru supported onto MWCNT (Ru/CNT)

The CNT-supported Ru nanoparticles were prepared by wet impregnation method. Typically, 0.5g CNT (CoMoCAT®) was added into the aqueous solution of RuCl$_3$ (200mg/10 mL H$_2$O) and then subjected to stirring for 1 h at room temperature. The solution was aged 2 h and after that the water was evaporated at 80°C. The catalyst was calcined at 350°C, in static atmosphere, for 4 h. The calcination temperature was established based on the TG analysis of CNT carrier (see Annex 1). The solid product was reduced in H$_2$ gas at 450°C for 2 h or using sodium borohydride (fresh aqueous solution) following a procedure from literature [30]. The metal loadings were ~1 wt %, ~3 wt % and ~5 wt % and the obtained samples were denoted 1%Ru/CNT, 3%Ru/CNT and 5%Ru/CNT.

3.1.2. MWCNTs oxidation

The oxidation of MWCNTs has the scop of the opening up of carbon nanotubes, their purification and fictionalization. Eight different oxidation procedures were performed in order to establish the optimum oxidation conditions in the view of the synthesis of an optimal functionalized CNTs structure. The prepared samples and the oxidation conditions are summarized in Table 1. For the first seven procedures CoMoCAT® MWCNT were used to produce the CNT$_{ox}$-1 - CNT$_{ox}$-7 samples while the CNT$_{ox}$-8 sample was produced from MWCNTs with 95% carbon, O.D×L/6-9 nm × 5 μm and armchair configuration. In order to minimize the tube damage, a low power sonicating bath and a relatively low acid exposure time were used. The oxidation processes were carried out either under reflux, by using a sonication bath or by refluxing followed by sonication. Nitric acid (65 wt%) or a mixture of HNO$_3$ and H$_2$SO$_4$ were used as oxidation reagents and the oxidation time was varied from 1h to 3h. Irrespective of the applied methodology the resulted solid was washed up to neutral pH and dried at 80°C for 24 h. All procedures methodologies are detailed in Annex 2.

Table 1. The oxidation conditions used for the synthesis of CNT_{ox} samples

Entry	Sample	m_{MWCNT} (g)	V_{HNO3} (mL)	V_{H2SO4} (mL)	V_{H2O2} (mL)	Procedure		
						Ultrasonication time (h)	Reflux	
							Time (h)	Temperature (°C)
1	CNT_{ox}-1	2	200	-	-	3	-	-
2	CNT_{ox}-2	1	200	-	-	3	2	80 (1h) 100 (1h)
3	CNT_{ox}-3	1	200	-	-	3	2	80
4[a]	CNT_{ox}-4	0.3	14	42	-	2	15 min	60
5[b]	CNT_{ox}-5	0.3	14	42	7.5	2	15 min	60
6	CNT_{ox}-6	0.1	7.5	-	7.5	3	15 min	60
7	CNT_{ox}-7	0.1	-	-	12.5	-	72	65
8[c]	CNT_{ox}-8	0.1	10	-	-	3	24	r.t.

[a] - 70 mL mixture of HNO_3 (65wt%) and H_2SO_4 (8M), mechanical stirring; [b] - 70 mL mixture of HNO_3 (65wt%) and H_2SO_4 (3M), mechanical stirring; [c] - distillation of CH_2Cl_2

3.1.3. Ruthenium based magnetic nanoparticles

The two steps preparation followed a literature reported procedure [31]: (a) the synthesis of the magnetic carrier that is comprised of spherically amino functionalized silica-coated Fe_3O_4 nanoparticles. In a typical procedure, 7 g of sodium dodecylbenzenesulfonate (technical grade, purchased from Acros Organics) was added in 60 mL dried xylene (purchased from Aldrich) and ultrasounded for 20 minutes, then stirred in an oil bath at room temperature. The air was removed from the reaction vessel by purging it with nitrogen. 3.23 g (8.0 mmoles) iron (III) nitrate nonahydrate and 0.8 g (0.4 mmoles) iron (II) chloride tetrahydrate were dissolved in 3.6 mL deionized water purged with nitrogen and added to the mixture of xylene and surfactant. The obtained mixture was stirred overnight under inert atmosphere at room temperature till homogenization. The emulsion was heated at 90°C, for 1 h, and then 4 mL of hydrazine 35% solution was added and stirred for 3 h, at 90°C and 1 h at 40°C, under inert atmosphere. Afterwards a mixture of 3 mL tetraethylortosilicate (TEOS, purchased from Aldrich) and 3 mL 3-aminopropyltriethoxysilane (purchased from Aldrich) was added and the

emulsion was stirred overnight in air atmosphere. The obtained black solution was transferred in a Berzelius flask and the obtained particles were separated with the aid of a Fe-Nd-B magnet. The separated particles were then washed five times with ethanol, recovered with a magnet, washed again with acetone and dried under vacuum. (b) the impregnation of the magnetic nanoparticles carrier with $RuCl_3$ solution in basic medium as follow: 2 g of Fe_3O_4–SiO_2/NH_2 were added to 200 mg $RuCl_3$ aqueous ruthenium (III) chloride (purchased from Aldrich) dissolved in 400 mL distilled water. The pH was adjusted at 13 with the aid of a NaOH aqueous solution (1M). The mixture was kept under stirring at 25 °C for 24 h. The solid was then magnetically collected from the solution, washed twice with distilled water and acetone and dried in vacuum.

3.2. Characterization techniques

Prepared samples were characterized by adsorption-desorption isotherms of liquid nitrogen at -196 °C, X-ray diffraction (XRD), temperature programmed desorption of H_2 and NH_3 (H_2-TPD and NH_3-TPD), IR diffuse reflectance with Fourier transform (DRIFT) and Raman spectroscopy, thermogravimetric-differential thermal analysis (TG-DTA) and scanning transmission electron microscopy (STEM).

Textural characteristics (surface area, pore volume and pore diameter) were determined from the adsorption-desorption isotherms of nitrogen at -196 °C using a Micromeritics ASAP 2020 Surface Area and Porosity Analyzer.

The morphology of the particles was analyzed using a scanning transmission electron microscopy (STEM) system. Bright field scanning transmission electron microscopy (BF-STEM) and dark field scanning transmission electron microscopy (DF-STEM) images were collected from Hitachi S-5500 operating at 30 kV accelerating voltage.

Powder X-ray Diffraction patterns were collected at room temperature using a Shimadzu XRD-7000 apparatus with the Cu Kα monochromatic radiation of 1.5406 Å, 40 kV, 40 mA at a scanning rate of 1.0 2θ min^{-1}, in the 2θ range of 10°–90°.

Hydrogen and NH_3-temperature programmed desorption (H_2- and NH_3-TPD) were recorded using a Micromeritics apparatus – Autochem II (Chemisorption Analyzer). Approximately 20 mg freshly reduced Ru/CNT was heated at 650°C under N_2 for 0.5 h to remove the hydrogen adsorbed on Ru atoms. After that, the temperature was reduced to 150°C and waited until baseline became stable. Subsequently, successive doses of H_2 gas (H_2-TPD) or NH_3 gas (NH_3-TPD) were provided. The NH_3-TPD measurements for CNTox samples were performed in the same manner.

DRIFT spectra were recorded with a Thermo 4700 spectometer (400 scans with a resolution of 4 cm^{-1}) in the range of 400–4000 cm^{-1}.

Raman spectra were recorded using a microscope equipped triple monochromator. The spectra were acquired in the back-scattering geometry, while for excitation the 514.4 nm line of an Ar$^+$ laser was focused on the sample by means of a 50 objective, measured directly.

TG-DTA analyses were recorded using a Shimadzu apparatus in a Pt crucible. The heating rate was of 10°C min^{-1}, respectively, starting from room temperature till 850 °C under a nitrogen flow of 50 mL min^{-1}.

3.3. Catalytic tests

The catalytic experiments were carried out in a stainless steel autoclave (15 mL, HEL Instruments). Briefly, to a solution of 25 mg lactic acid in 10 mL NH$_3$.H$_2$O (solution of 28 wt%), 5-50 mg of catalyst was added. The resulted mixture was stirred at 180-250°C, under 10 atm of H$_2$ and for 0.5-8h. After reaction the autoclave was quickly cooled at room temperature, the catalyst was recovered by centrifugation and the products were separated by solvent distillation under vacuum. Two blank reactions in which a solution of 25 mg of lactic acid in 2.5 mL NH$_3$.H$_2$O (solution of 28 wt%) was maintained at 200°C, in the presence (10 atm of H$_2$) or absence of hydrogen and for 2h were also performed. Also, two reactions in which 25 mg of lactic acid in water or in 2.5 mL NH$_3$.H$_2$O (solution of 28 wt%) was maintained under stirring, at 180°C for 2h.

The recovered products were silylated (200 µL of a derivatization agent (1% w/w of trimethylchlorosilane in N,O-Bis(trimethylsilyl)-trifluoroacetamide) and 200 µL of pyridine, 80 °C for 4 hours), diluted with 1 mL of ethyl acetate and analyzed with a GC-MS Carlo Erba Instruments (Waltham, MA, USA) QMD 1000 equipped with a Factor Four VF-5HT column (0.32 mm x 0.1 mm x15mm).

The lactic acid conversion (X) and selectivities (S$_n$) to reaction products n were calculated from the chromatographic analysis by using the follow equations:

$$X\% = \frac{n_i - n_t}{n_i} \, x100 \qquad S_n\% = \frac{Yield_n}{X} \, x100$$

Where: n_i – initial moles of lactic acid; n_t – moles of untransformed lactic acid at time "t", determined from chromatographic analysis

4. Results and discussions

4.1. Ru/CNT samples characterisation

Liquid nitrogen adsorption-desorption isotherms at -196°C

  Figures 6-8 show the nitrogen adsorption-desorption isotherms at -196 °C and the corresponding pore size distribution obtained through the Barret–Joyner–Halenda (BJH) method for the 1%, 3% and 5%Ru/CNT samples.
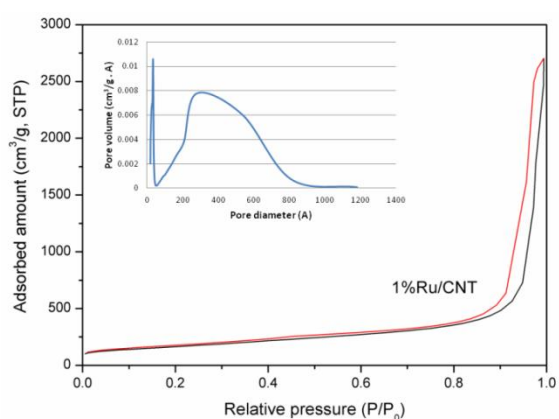

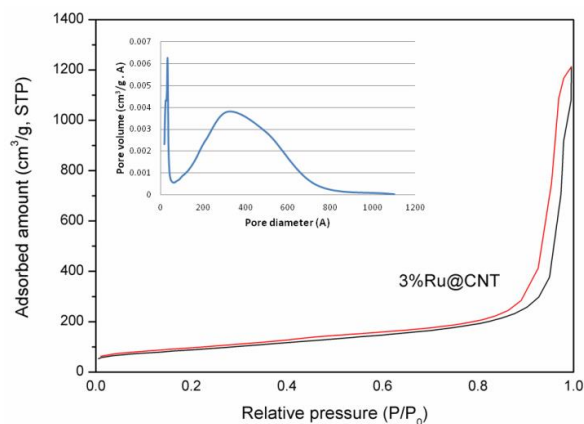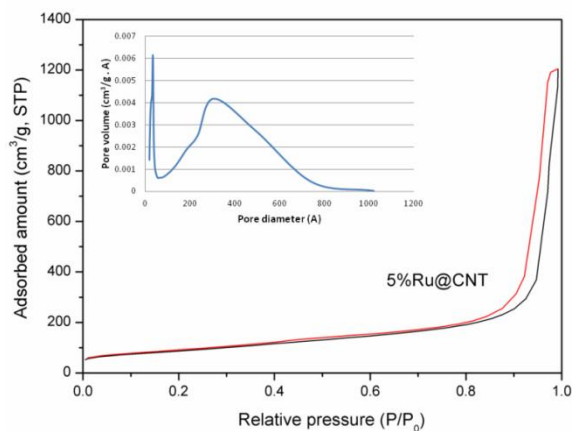**Figure 6.** Nitrogen adsorption-desorption isotherm and pore size distributions (inset) for 1%Ru/CNT sample

Figure 7. Nitrogen adsorption-desorption isotherm and pore size distributions (inset) for 3%Ru/CNT sample

Figure 8. Nitrogen adsorption-desorption isotherm and pore size distributions (inset) for 5%Ru/CNT sample

The pore structure parameters of Ru/CNT sample determined by BET, t-plot and BJH methods are summarized in Table 2. The specific surface area (S_{BET}), the total pore volume (V_p) and the porosity of the samples are presented in Table 2. The specific surface area (S_{BET}) of the samples was calculated following the BET (Brunauer–Emmett–Teller) procedure with eight relative pressures (p/p_0) of nitrogen in the range of 0.07–0.2. The t-plot method was used to determine the micropore and external surface area and also the micropore volume. The Barret–Joyner–Halenda (BJH) method was used to determine pore size distribution, considering the desorption curves.

Table 2. The pore structure parameters of Ru/CNT sample determined by BET, t-plot and BJH methods

Entry	Sample	S_{BET} (m²/g)	Micropore surface area (m²/g)	External surface area (m²/g)	Total pore volume (cm³/g)	Micropore volume (cm³/g)	Mezopores volume (cm³/g)	Avarage pore size (BJH, nm)
1	1%Ru	584	56	527	3.82	0.02	3.80	3.3 and 27.7
2	3%Ru	315	22	293	1.67	0.01	1.66	3.3 and 31.9
3	5%Ru	310	20	291	1.88	0.01	1.87	3.3 and 30.5

All the nitrogen adsorption-desorption isotherms (Figures 6-8) can be divided in four parts as shown in Figure 9, indicating a multistage adsorption process.

In part I (around p/p_0 of 0.01), the isotherm is normally of type I characteristic indicated by the fact that the nitrogen adsorption amount increases at ultra-low pressure. Such a process occurs in pores with molecular size, suggesting that in the samples there are micropores contributed by the opened inner cavities in the CNT with very small diameter. Nitrogen molecules, whose diameter is about 0.364 nm, can fill in these pores under ultra-low adsorption pressure. However, as Figure 9 shows, in the case of our samples, there is only a very slightly increased amount of nitrogen adsorption in this portion of isotherms. Table 2 shows both very low micropores surface area and micropores volume. Part II of the isotherms (p/p_0 = 0.01-0.4) shows a slowly increases of the nitrogen adsorption amount with the formation of the surface monolayer.

A hysteresis loop is clearly visible in part III and IV of the isotherm, associated with the capillary condensation in mesopores [32]. These ranges show Type IV isotherm characteristics. Part III corresponds to capillary condensation occurring at medium relative pressure range (p/p_0 = 0.4-0.85) in

small mesopores with a size of 3.3 nm (Table 2, column 9), which is similar to the inner cavity diameter of the pristine opened CNT [33]. As Table 2 shows this size remains constant, irrespective of the ruthenium concentration, indicating a lack of ruthenium deposition during the impregnation process in the inner hollow cavity of the CNT.
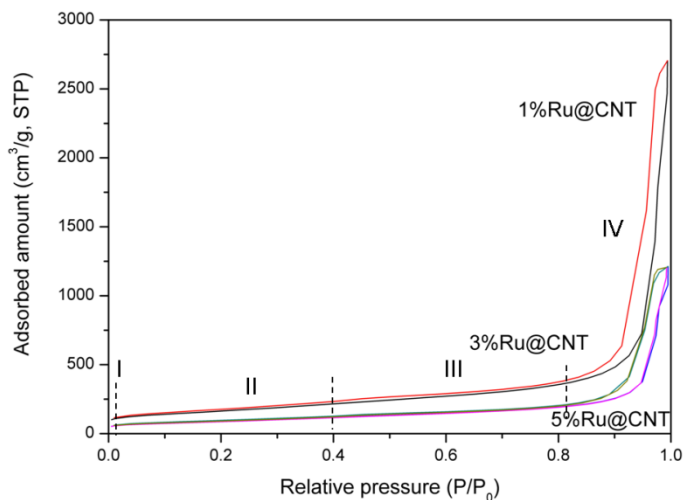

Figure 9. Nitrogen adsorption-desorption isotherms of Ru/CNT samples

When the pressure nears to the saturation pressure (part IV of the isotherm, $p/p_0 = 0.85$-0.99), the adsorption amount shows a great increase, indicating a strong capillarity in larger mesopores. In MWCNTs these hysteresis loop (H3 type) correspond to pore size of about 20-40 nm which is likely to be contributed by aggregated pores since there are not CNT with so large inner cavity diameter and, accordingly, to form so big inner porosity [33]. Therefore, the so-called aggregated pores are formed by the confined space among the isolated nanotubes of different orientation which interacts by inter-molecular force creating a relatively stable aggregated structure (Figure 10).
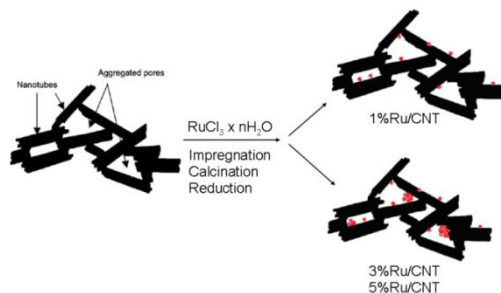
Figure 10. Schematic structural model for the aggregated pores in CNTs adapted from [13] and the structural models of the Ru/CNT samples

22

The corresponding pore sizes to aggregated pores in Ru/CNT samples slightly vary in a range of 27.7-31.9 nm (Table 2). This variation, along with the decreases of the external surface area clearly indicates the deposition of the ruthenium take place on the outer side of the CNT tubes. Moreover, the high difference between the S_{BET} of the 1%Ru/CNT sample (Table 2, entry 1) and the S_{BET} of the 3%Ru/CNT and 5%Ru/CNT (Table 2, entries 2 and 3), respectively, indicates a high uniform deposition, with a high dispersion degree, of the ruthenium particles for the 1%Ru/CNT sample and a high agglomeration of the ruthenium particles in the case of the last two samples (Figure 10). These results are in agree with Chu and co-workers which showed not long ago [34] that the main Ru particle size is smaller if ruthenium is deposited on the inner surface of the carbon nanotubes (denoted Ru-in-CNTs) than that of deposited ruthenium on the external surface of the nanotubes (denoted Ru-out-CNTs), indicating that particle sintering is prevented in Ru-in-CNTs under the reduction condition due to the spatial restriction of the CNT channels. The narrower size of the aggregated pores in the case of the 1%Ru/CNT sample also indicates a slightly denser packaging of the CNT network, again confirming the high uniform deposition of the ruthenium particles in the case of this sample. The agglomeration of the Ru particles on the outer walls of CNT for high concentrations of ruthenium (i.e., 3% and 5%, respectively) is also confirmed by XRD and STEM measurements.

X-Ray diffraction (XRD)

The X-ray diffraction (XRD) patterns of the as-synthesized Ru/CNT powders were recorded to examine their phase purity and crystallinity. As shown in Figure 11, CNT has two characteristic reflection lines at 26° and 43.9°, corresponding to the (002) and (100) facets, respectively, according with literature data [35, 36]. The line from 26° indicates that the spacing between the sp^2-C layers in the multi-walls CNTs is 0.343 nm [35]. As the XRD pattern of the CNT carrier shows the impregnation of the CNTs with different quantities of ruthenium salts and the activation steps does not damaged the CNT structure.

In the case of 1%Ru/CNT sample no diffraction lines corresponding to ruthenium particles are evidenced suggesting the formation of nanoparticles with narrow size and high dispersion for this sample (Figure 11, spectrum in black). However, for the samples 3%Ru/CNT and 5%Ru/CNT, apart from the lines characteristic to the CNT carrier, some characteristic lines corresponding to the Ru (hexagonal phase; JCPDS Card No. 06-0663) at 38.3°, 42.8°, 58.4°, 69.6° and 78.7°, assigned to (100), (101), (102), (110) and (103) reflections of metallic Ru are evidenced [37]. This indicates an

agglomeration of the ruthenium species during the samples preparation with the formation of larger ruthenium particles.
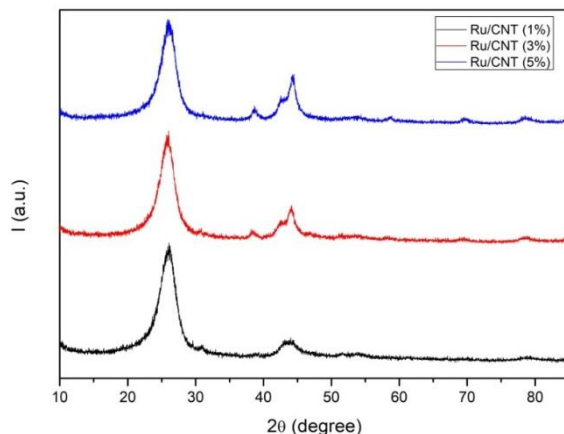

Figure 11. XRD patterns of different Ru-based CNTs catalysts

The average size of ruthenium crystallites was determined from the Debye-Scherrer equation taking the (100) reflection of ruthenium particles [38]:

$$d = \frac{k\lambda}{\beta \cos \theta}$$

Where: d is the crystallite size in nm; k = 0.94; λ is the wavelength of the X-ray (1.54178 Å); θ is the half-diffraction angle and β is the full width at half-maximum (FWHM) in radians for the 2θ value (38.3°).

The ruthenium particles size diameter is 9.0 nm for the 3%Ru/CNT sample and 10.6 nm for the 5%Ru/CNT sample.

Scanning transmission electron microscopy (STEM)

Scanning transmission electron microscopy (STEM) was used in order to describe the morphology of the ruthenium nanoparticles. Bright field and dark field images were collected at different resolutions in order to see better the dispersion of metals onto the external surface of the carbon nanotubes. For each loading (1wt%, 3wt%, 5wt%) were selected three images. The average diameter of the particle was calculated using a graphical method, taking into account minimum 10 ruthenium nanoparticles.

For the sample 1%Ru/CNT, as it can be seen from Figure 12, we observe that the distribution of ruthenium nanoparticles is uniformly. The ruthenium particles, with an average size of 2.5 nm, are deposed on the external surface of the carbon nanotubes and no agglomeration is present.
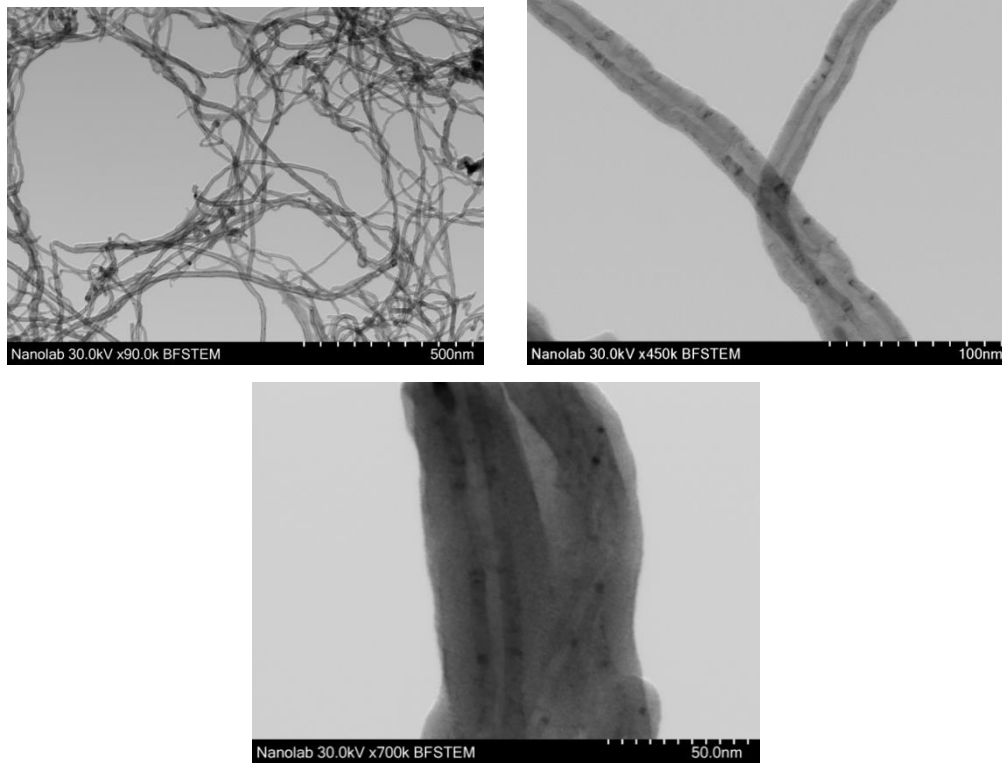

Figure 12. BF-STEM images for the 1%Ru/CNT sample

For the sample 3%Ru/CNT, as can be seen from Figure 13, the distribution of ruthenium nanoparticles in still uniform. The ruthenium particles are deposed on the external surface of the carbon nanotubes and a slightly agglomeration is present. The average particle size is 5.0 nm this being expected because it is well known that the particles aggregate as the metal loading increases.

For the sample 5%Ru/CNT, as can be seen from Figure 14, the distribution of ruthenium nanoparticles is uniform until some extent. A few particles agglomeration was observed but the deposition on the external surface of the carbon nanotubes is preserved. The average particle size is 7.0 nm.
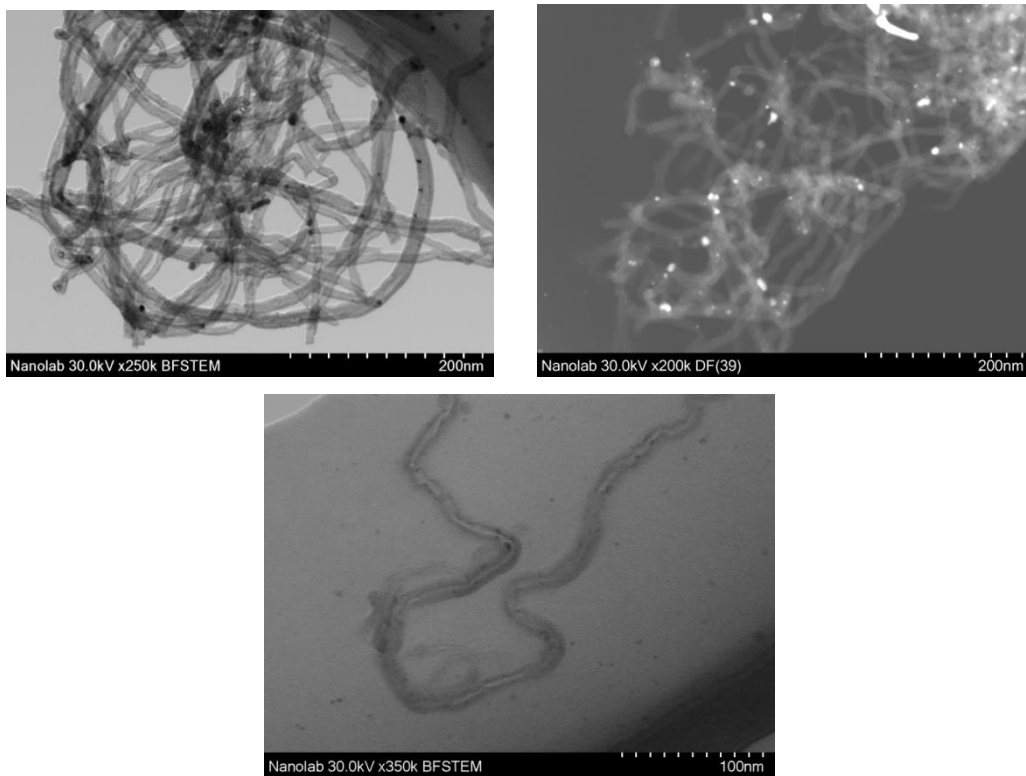
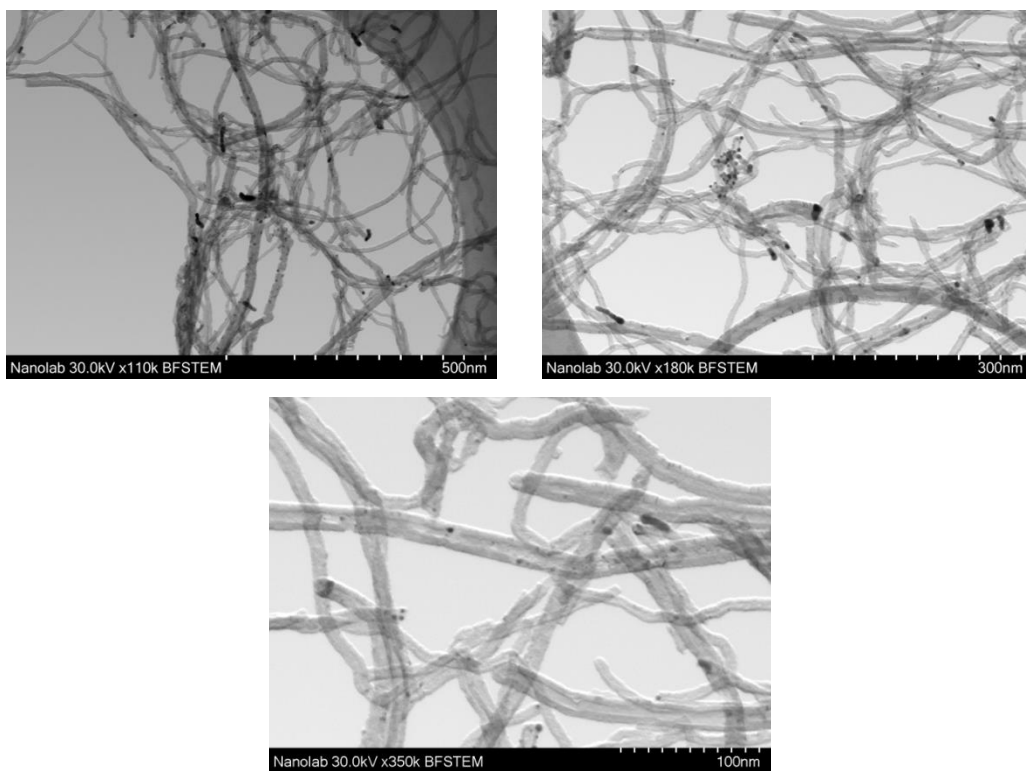**Figure 13**. BF and DF-STEM images for the 3%Ru/CNT sample

Figure 14. BF-STEM images for the 5%Ru/CNT sample

NH₃-TPD

Chen et al. [39] reported that the deviation of the CNT graphene layers from planarity causes p-electron density shifting from the concave inner surface to the convex outer surface, leading to an electron deficient internal surface and an electron-enriched external surface. This electron density loss is partially compensated through the interaction with the encapsulated metal [40] which would destabilize the metal nanoparticles and facilitate their reduction. In connection with this statement and with the findings from the previously results obtained from the characterization techniques applied for the elucidation of the structural and chemical characteristics of the Ru/CNT samples, temperature programmed desorption of ammonia (NH_3-TPD) was performed to assess the acid properties of the CNTs support and corresponding Ru-based catalysts. It is well known the oxide form of the noble metals display Lewis acid characteristics. The existence of the Brønsted acidity should also does not be excluded through the possibility of the -OH groups existence, anchored on the oxide particles.

The temperature of maximum desorption rate, i.e., the temperature of a TPD peak, is used as a measure of the acid strength of the sorption sites. The method has the limitation that it can distinguish sites by sorption strength but not Lewis (L) from Brønsted (B) type sites. However, for zeolites there are several literature reports which divide desorption regions in two, bellow and above 400°C, referring to low-temperature (LT) and high-temperature (HT) regions, respectively [41]. The peaks in the HT region are attributed to the desorption of NH_3 from strong B and L sites while the assignment of the LT peaks is still controversial [41]. The possibility that weak L acid sites were responsible for the LT peak was considered [42] but the release of NH_3 hydrogen-bound to NH_4^+ cations were also not excluded [43]. The NH_3-TPD profiles of the CNT and Ru/CNT samples are given in Figure 15.
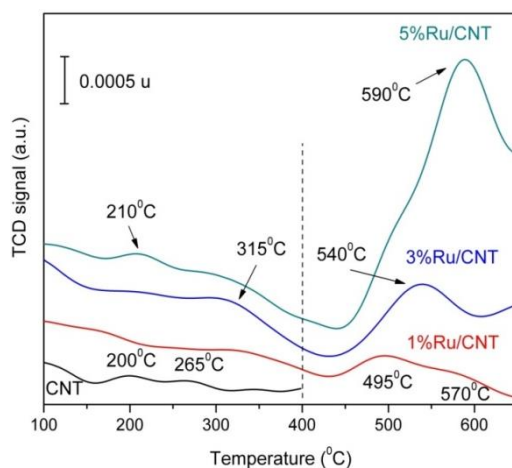

Figure 15. NH_3-TPD profiles for the Ru/CNT samples

As Figure 15 shows, the CNT carrier contains only an insignificant amount of acid sites, situated in the LT region. However, their impregnation with ruthenium salt followed by calcination and reduction leads to the appearance of acid sites, their highest concentration being in the HT region. Moreover, the higher the ruthenium concentration the higher the concentration of the L and B acid sites. Nevertheless, the level of the acid site concentration is very low and vary from around 0.4 µmol/g (1%Ru/CNT) to 2.2 µmol/g (5%Ru/CNT).

As previously shown, the obtained results from the nitrogen adsorption-desorption isotherms, XRD and STEM measurements clearly indicate that ruthenium particles are deposited on the external surface of the CNT tubes. However, if in the case of 1%Ru/CNT sample, small ruthenium particles with a high dispersion are formed, for samples with 3% and 5%Ru, the formation of larger particles with a low dispersion is also observed. In agree with Wang et al. [44] such large particles are hardly reduced. Therefore, the new peaks from the NH_3-TPD profiles of Ru/CNT (Figure 15) could be assigned to a partial reduction of Ru^{3+} to Ru^0 species with the formation of some RuO_x-OH species alongside the metallic particles.

H_2-TPD

The effect of reduction temperature on catalytic behavior has been the subject of many investigations. Many studies have shown both reduced catalytic activity and reduced hydrogen chemisorption capacity after reduction in hydrogen at high temperatures (> 500°C) but a clear understanding of the phenomena involved is still lacking. Reduction at high temperatures may result in strongly chemisorbed hydrogen, may cause loss of spillover hydrogen altering the local charge transfer from the support to the metal at the particle boundary, may induce changes in morphology of the metal crystallite and may affect reduction of the support leading to the formation of an alloy with atoms from the support [45].

In this study the temperature-programmed desorption of hydrogen was performed in order to check the strength of metallic ruthenium interactions with hydrogen. Therefore, the H_2-TPD spectra of previously reduced (450°C) Ru/CNT samples were measured. The maximum desorption temperatures and corresponding desorbed amount of hydrogen are given in Table 3.

The maximum of the hydrogen desorption peak found in this study for CNT carrier is lower than that for graphite (143°C versus 207°C) [46], suggesting a lower binding energy of the hydrogen

adsorption in the case of CNT. Many authors claim that hydrogen molecules mostly adsorb on the outer surfaces of CNT and the reduction in binding energy value is generally attributed to the surface curvature [47].

Table 3. H_2-TPD parameters for Ru/CNT samples and CNT carrier

Entry	Catalyst	H_2 desorbed (mmol/g)	Peak temperature (°C)
1	CNT	1.18	143
2	1%Ru/CNT	0.010	328
		0.008	340
		0.008	370
	Total	**0.026**	
3	3%Ru/CNT	0.003	290
		0.005	310
		0.008	390
		0.004	520
	Total	**0.020**	
4	5%Ru/CNT	0.002	590

The hydrogen desorption begins at 200°C for all Ru-based catalysts. However, the maximum desorption peak depends on the ruthenium concentration. For catalysts with 1% and 3%Ru the H_2-TPD profiles comprise three or more peaks (the maximum temperature for these peaks are given in Table 3) owing to the formation of various active sites or to the effect of spillover hydrogen, while for 5%Ru/CNT sample, the only one maximum desorption peak was visible at 590°C. The peaks at the desorption temperature lower than 500°C (1% and 3%Ru) can be attributed to the dissociative adsorbed hydrogen and spillover hydrogen simultaneity, while the peak at above 500°C (3% and 5%Ru) can be associated to the spillover hydrogen stabilized by hydroxyl groups from the ruthenium oxides surface. A low temperature of the hydrogen desorption indicates, therefore, a weaker adsorption of H_2 and its greater mobility on the catalyst surface while a high temperature for the hydrogen desorption indicates a strongly chemisorbed hydrogen [48]. Based on H_2-TPD results, the mobility of hydrogen on the surface of catalysts can be ordered in the following sequence: 1%Ru/CNT > 3%Ru/CNT > 5%Ru/CNT. Moreover, the higher the ruthenium concentration the lower the hydrogen desorbed

amount. These data are also in agree with the NH₃-TPD results according to which the higher the amount of ruthenium the lower the reduction degree of the agglomerated ruthenium particles.

DRIFT spectroscopy

It should be noted that the spectrum of the pristine CNT is quite similar to others presented in the literature [49]. Some claimed MWCNT-specific infrared (IR) spectral features include peaks associated with O−H vibrations (1600 and 3740 cm^{-1}), carboxylic groups (1740 cm^{-1}), -C=C-stretching vibration (1523 cm^{-1}) and C−H stretching vibrations (close to 3000 cm^{-1}), even though they correspond to defects and impurities rather than the MWCNT structure itself (Figure 16). The most important use of infrared spectroscopy in MWCNT research is the characterization of surface functionalization [50] and this will be discussed in the next section.

The infrared spectra of the CNT and Ru/CNT samples are given in Figure 16. Similar peaks were identified for all samples. However, in the case of Ru/CNT samples a new peak at 3630 cm^{-1} was identified into the corresponding spectra, associated with possible O-H vibrations from RuO_x-OH groups.
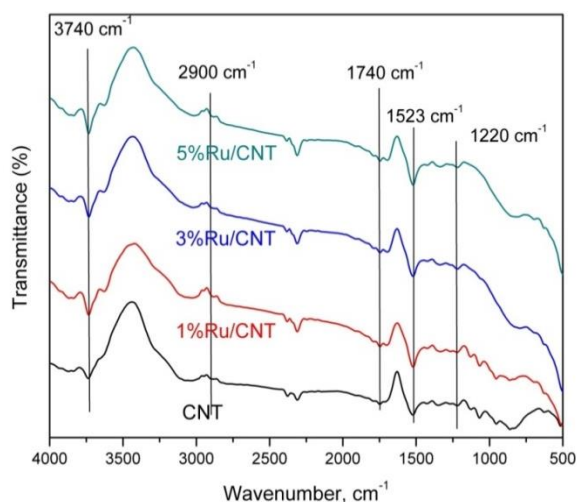

Figure 16. IR spectra of the CNT and Ru/CNT samples

4.2. *Oxidation of CNTs: Opening up of carbon nanotubes, purification and functionalisation*

As the nitrogen adsorption-desorption isotherms of the Ru/CNT samples showed, the capillarity mainly occurs in the small cylindrical mesopores (inner cavities) and the aggregated pores of CNT, the latter being associated with the larger portion of the total nitrogen adsorption amount. The small

fraction of the total nitrogen adsorption amount in the inner cavities (Figures 6-9) indicate that not all ends of nanotubes are opened [33]. However, to improve the adsorption and capillarity of CNTs both the opening-up of the nanotubes and the control of their aggregated pore texture is important.

The simplest method to open nanotubes is their oxidative treatment. It is well known that graphite oxidizes primarily at defects of the hexagonal lattice to create etch pits. When such defect sites are present in the wall of the nanotubes, they become the center of preferential etching. However, nanotubes have additional structural features such as high curvature and helicity, and may contain five- and seven-membered rings, which modify the initiation and also the propagation of oxidation. Particularly for MWCNTs, the oxidation tends to start near the tips, providing a mechanism for opening the tubes.

Oxidative treatment of nanotubes results not only in nanotubes open at their tips, but also nanotubes that are thinner in diameter [51]. The concentric layers of MWCNTs do not react at the same rate, since each shell has its own tip. It follows that the inner shells might persist longer than the outer ones. Therefore, different oxidation rates are assumed for oxidation of an open MWCNTs. The extent of the thinning depends on the duration of treatment.

A further consequence of oxidative treatment is the partial functionalization of the tubes, i. e., the nanotubes become covered with carboxyl or hydroxyl groups at their ends. These functional groups make the NTs partially soluble. The number or concentration of the inserted carboxyl groups can be estimated by acid–base titration or NH_3-TPD. The concentration of the surface acid groups on nanotubes opened by various oxidants is in the range of 2×10^{20}–10×10^{20} sites per gram of nanotube [52].

XRD

In case of carbon nanotubes, after some authors, the resolution of the XRD diffraction pattern is a complex matter because of the extremely large variation in their size, curvature and the disorder in the packing of the graphene sheets. [53] All these factors combined together affect the reflectance, as well as diffraction line positions and widths from one sample to another.

The X-ray pattern for the pristine CNTs (Figure 17, inset) presents a sharp well defined diffraction line at $2\theta = 25.8°$ and one smaller line at $43°$, corresponding with (002) and (101) planes. According to literature [55] the diffraction line from $25.8°$ correspond to the spacing between graphene sheets. Besides these out-of-plane ordering reflectance, CNTs also show two lines at 2θ values of $28°$

and 52° respectively, corresponding with (100) and (102) planes. However, in this case, the XRD pattern does not present the out-of-plane reflectance and in-plane reflectance, thus implying the lack of in-plane ordering in these specific directions. Subsequent to acid treatment, the XRD spectra show a change in the magnitude and the 2θ shifting position of the reflectance lines (Figure 17).

In the case of CNT_{ox}-1, CNT_{ox}-2 and CNT_{ox}-3 samples the intensity of the line at $2\theta = 25.8°$ is higher than that of the pristine CNT, this increases being attributed to an increase in the number of walls of the CNTs [56]. In the case of CNT_{ox}-4, CNT_{ox}-7 and CNT_{ox}-8 the intensity of the line at $2\theta = 25.8°$ is lower than that of the pristine CNT, being attributed to a decrease in the number of walls of the CNTs. The lower intensity has also been related to a lower packing density or the presence of defects. Not less important, the decrease in the intensity of the (002) plane ($2\theta = 25.8°$) is also attributed to the disordered structure of the nanotubes. This disorder is the effect of the attachment of functional groups at the surface and ends of the nanotubes, thus causing steric hinderance and impelling the individual nanotubes to misalign. The comparatively greater height of the (002) plane ($2\theta = 25.8°$) in case of as-received CNTs has also been explained in terms of the greater graphitic character of the tubes [53]. This may only be true if there are a large number of equidistant tubes in the MWCNT so that their reflectances overlap to five a high intensity line.
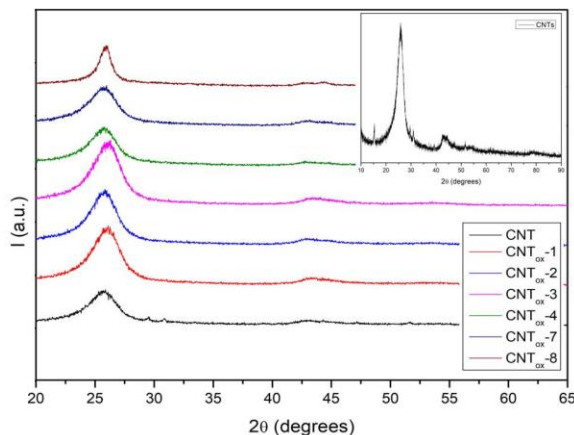

Figure 17. XRD pattern of as-received MWCNTs and oxidised CNTs

The shifting of the (002) plane ($2\theta = 25.8°$) toward higher values of 2θ angle from as-received CNTs until CNT_{ox}-8 is a result of an decrease in the intertubular spacing, which in turn indicates a loss in the ordered structure of the nanotubes.

The X-ray diffraction patterns of oxidized CNTs show a relatively greater broadness of the line at 43.3° indicating a lower crystallinity and a greater curvature in the nanotubes surface. According to

literature [54], the greater the diameter of CNTs the smaller is its curvature, thus resulting in a larger value of the d-spacing which, in this case, implies a smaller diameter of the tubes.

The broader distribution of lines in CNT_{ox}-5 and CNT_{ox}-6 as compared to the as-received CNTs reflects the turbostratic character of the nanotubes (Figure 18). This is because the debundling of CNTs decreases the crystalline domains size, resulting in the increased amorphous character of the nanotubes. It has also been reported that a broader distribution of d-spacing results in broader peaks [55] which is also a direct consequence of over-oxidation and loss of graphitic character.

.
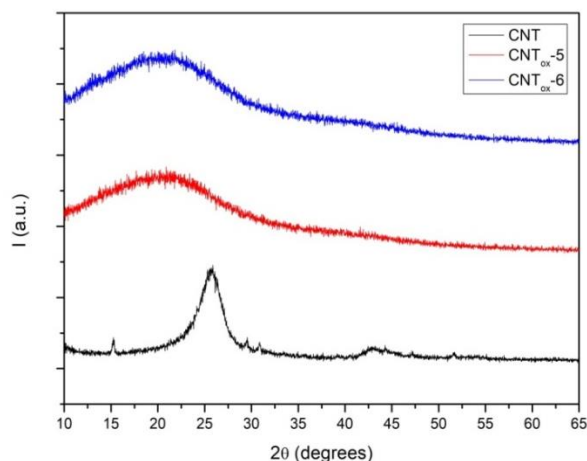
Figure 18. XRD patterns of oxidized (5-6) MWCNTs and as-received MWCNTs for comparison

NH₃-TPD

It is known that the amount and type of oxygen-containing functional groups strongly depends on the treatment methods and their process parameters. In case of nitric acid, the nitronium ion NO_2^+ is believed to be able to attack the aromatic compounds, which is assumed to be the first step in the generation of oxygen-containing functional groups, followed by the formation of carbonyls and their conversion into carboxylic groups and carboxylic anhydrides [56]. In addition, nitrogen-containing groups can also be created by the nitric acid treatment.

Figure 19 shows the NH₃-TPD profiles for the CNT_{ox} samples obtained by HNO₃-treated nanotubes in different conditions (for oxidation conditions see Table 1).
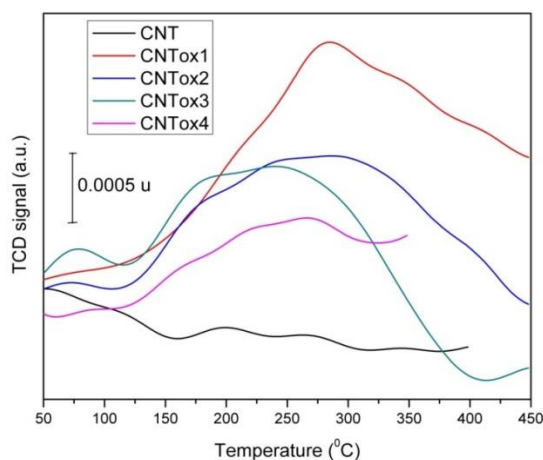
Figure 19. The NH3-TPD profiles of the CNT$_{ox}$ samples

The main ammonia TPD peak appeared at about 260-280 °C (Figure 19), indicating that most of the ammonia molecules are chemisorbed with a medium strength. The shoulder at high temperatures (cca 400°C, CNT$_{ox}$-1 and CNT$_{ox}$-2 samples) can be assigned to carboxylic structures, onto which ammonia chemisorbs strongly presumably *via* the formation of ammonium carboxylates. Most of the acidic groups act as primary adsorption centers, which bind additional ammonia molecules weakly through hydrogen bonds [57].

The total desorbed ammonia (mmol/g) varied in order: 0.073 (CNT$_{ox}$-2) > 0.053 (CNT$_{ox}$-1) $\geq$0.052 (CNT$_{ox}$-3) >> 0.004 (CNT$_{ox}$-4), which strongly depends on the oxidation procedure conditions.

IR spectroscopy

In Figure 20, IR spectra of the CNTs before and after the oxidation process (CNT$_{ox}$-1 - CNT$_{ox}$-4) are presented. The presence of typical C=O and O-H bonds are due to the formation of COOH groups on the nanotubes after acid treatment. This is evident in the IR spectrum shown in Figure 20. Different peaks at 3600-3900 cm^{-1} are assigned to the O-H stretches of terminal carboxyl groups, the peaks at 2800-2944 cm^{-1} can be assigned to the C-H stretch, and the peaks near 1742 cm^{-1} correspond to the carboxylic C=O stretching vibrations. The peak at 1527 cm^{-1} is attributed to the -C=C- stretching mode of the CNTs [58]. IR spectra also indicates the presence of the carbonyl (C=O) (1223 cm^{-1}) groups and the presence of the epoxide groups indicated by the presence of an absorption band in the 910-920 cm^{-1} range, related to the contraction of the C-C bond and the stretching of C-O bonds of the epoxy ring [59].
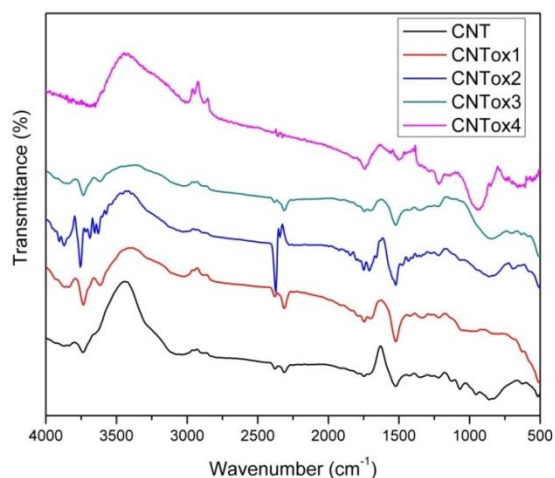
Figure 20. IR spectra of CNT and oxidised CNTs samples

(see procedures 1-4 from Annex 2).

The highest amounts of -COOH and carbonyl groups were generated on $CNT_{ox}5$-7 (Figure 21). Unfortunately, a too advanced oxidation lead to a structure collapse as XRD analysis show for the CNT_{ox}-5 and CNT_{ox}-6 samples. Indeed, the IR spectra also shows a high increases of the bands intensity corresponding to the C-H stretch (2800-2944 cm^{-1}) and of those corresponding to the contraction of the C-C bond (910-920 cm^{-1} range) in the detriment of the -C=C- stretching mode (1527 cm^{-1}).
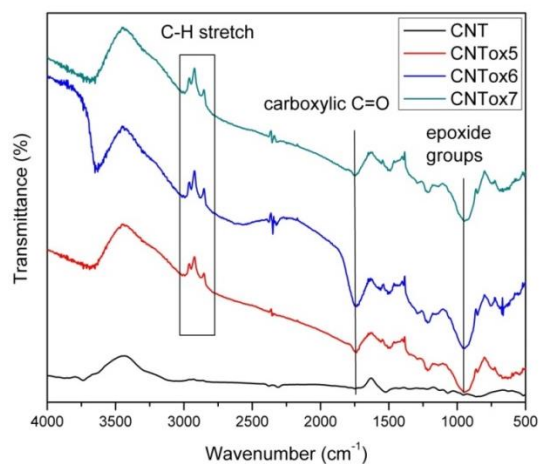
Figure 21. IR spectra of CNT and oxidised CNTs samples

(see procedures 5-7 from Annex 2).

Raman spectroscopy

Raman spectroscopy is a very valuable tool for the characterization of carbon-based nanostructures. The Raman spectrum of as-received CNTs is shown in Figure 22.
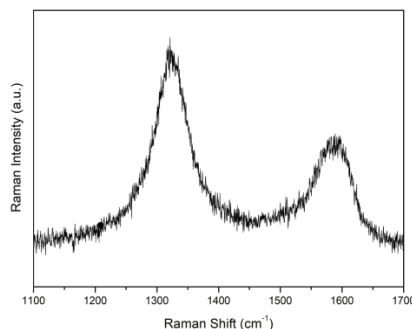

Figure 22. Raman spectra for as-received MWCNTs (i.e., CNT sample)

The Raman spectrum consists of three characteristic bands: D band, G band and D' band. In the as-received carbon nanotubes the D band appears at 1322 cm^{-1}, the G band appears at 1587 cm^{-1} and the D' band appears at 1606 cm^{-1}. The D-band is a disordered induced feature, arising from double resonance Raman scattering process from a non-zero centre phonon mode [60]. The D band is usually attributed to the presence of amorphous or disordered carbon in the CNT samples. The carbon structural disorder is due to the finite or nanosized graphitic planes and other forms of carbon such as rings along with defects on the nanotube walls. The G band originates from in-plane tangential stretching of the carbon-carbon bonds in graphene sheets [60]. The D' band, which appears as a weak shoulder in the G band at higher frequencies, is also a double resonance feature induced by disorder and defects. Also, it should be underlined that the radial breathing modes are too weak to be observed due to the large diameters of the tubes.

The Raman spectra obtained for some of oxidised CNT samples are shown in Figure 23. A slightly up-shift for the G band, indicating an increases of the number of sp^2 carbons, is observed from CNT_{ox}-1 toward the CNT_{ox}-7 sample. This effect usually indicates the strength of the oxidation process: the greater the displacement the stronger the oxidative process. Therefore, CNT_{ox}-7 sample is stronger oxidised than the CNT_{ox}-1 sample. This statement is in agreed with the results obtained from DRIFT measurements (Figures 20-21).
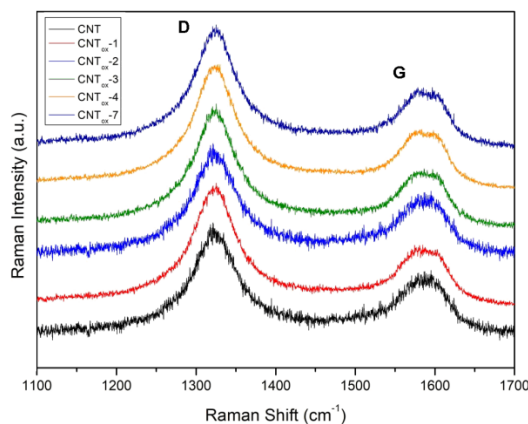
Figure 23. Raman spectra for as-received and oxidized MWCNTs from 1-4 and 7

The Raman spectra of the CNT_{ox}-5, CNT_{ox}-6 and CNT_{ox}-8 samples are presented in Figures 24 and 25. As Raman spectra of CNT_{ox}-5 and CNT_{ox}-6 samples (Figure 24) shows an up-shift of the D band and a slightly decrease in intensity for D and G bands takes place, most probably due to an over oxidation of the CNTs according to Chernyak S.A. and al. [61]. This over oxidation also lead to an increased amorphous character of the nanotubes, as corresponding XRD patterns showed (Figure 18).

In the Raman spectrum for CNT_{ox}-8 (Figure 25) a decrease in the wavenumber of the G band accompanied by an increase in the wavenumber of the D band is visible. Moreover, the D' band, corresponding to the defects in the CNT structure is more visible. These new features of the Raman spectra suggest a successful synthesis of an oxidized CNT with a concomitant increase in the number of defects compared to pristine CNT.
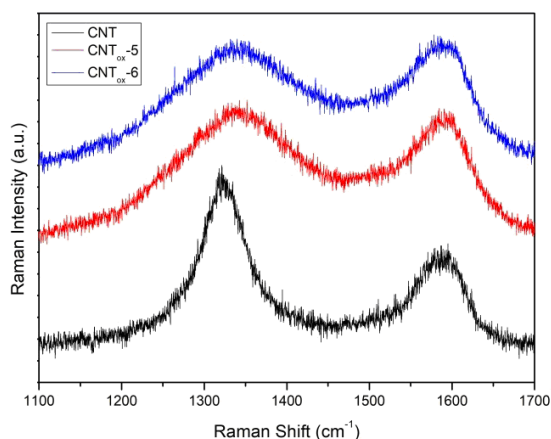

Figure 24. Raman spectra for as-received CNT and CNT_{ox}-5 and CNT_{ox}-6 samples
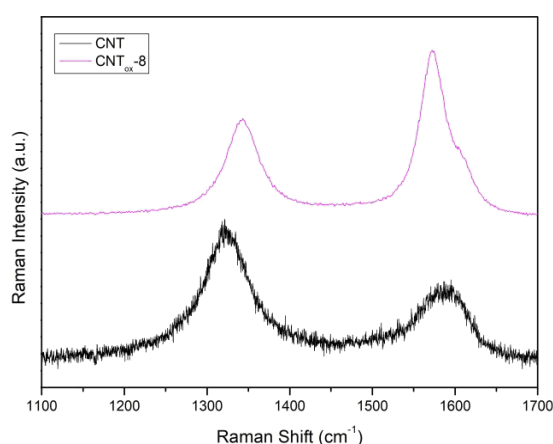

Figure 25. Raman spectra for as-received CNT and CNT_{ox}-8 sample

The intensity ratio of G to D band in the Raman spectra of oxidized samples is presented in the Table 4.

Table 4. I_G/I_D intensity ratios for the treated CNTs

Sample	Pristine	CNT_{ox}-1	CNT_{ox}-2	CNT_{ox}-3	CNT_{ox}-4	CNT_{ox}-5	CNT_{ox}-6	CNT_{ox}-7	CNT_{ox}-8
I_G/I_D	0.63	0.38	0.21	0.37	0.43	0.96	1.01	0.34	1.66

As Table 4 shows the intensity ratio G to D band (I_G/I_D) is almost the same indicating a similar defect population for the CNT_{ox}-1, CNT_{ox}-3 and CNT_{ox}-7 samples. However, compared to the as-received CNT, the I_G/I_D ratio of these samples is considerable lower, indicating a destruction of the graphitic integrity and the subsequent formation of small graphitic fragments. A I_G/I_D ratio of around 1.0 indicates a fully oxidation of the CNT_{ox}-5 and CNT_{ox}-6 samples, while the higher intensity ratio I_G/I_D for CNT_{ox}-8 compared with the pristine CNT indicate the highly increased of the defects population.

TG-DTA

It is well known that different structural forms of carbon can exhibit different oxidation behaviour depending on the available reactive sites. For instance, disordered or amorphous carbons tend to be oxidised at around 500°C [53] because of their lower activation energies for oxidation or due to the presence of a large number of active sites. On the other hand, a well graphitized structure starts to oxidize at a relatively higher temperature, as a function of the type of CNTs.

The thermogravimetric measurements conducted on the as-received CNTs and on the oxidized samples CNT_{ox} 1-8 are presented in Figure 26. As expected, the thermal degradation of MWCNT is a multistage process. The first step, up to a temperature of 150°C, shows a weight loss of 1-5% for the highly hydrophilic nitric acid-treated CNTs samples and for the CNT_{ox}-4 (nitric acid/sulphuric acid), which corresponds to the evaporation of the adsorbed water. The second step, from 150°C to 350°C is attributed to the decarboxylation of the carboxylic groups present on the CNTs walls. This second step appears in all the samples treated with nitric acid but do not appear in the samples treated with H_2O_2.
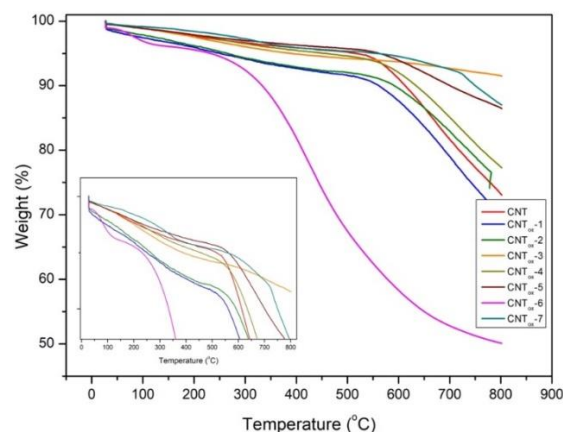
Figure 26. TGA profiles in N_2 atmosphere for CNT_{ox} 1-8 and as-received CNTs for comparison

Thermal degradation in the range of 350-500°C may be explained by the elimination of hydroxyl functionalities attached to the CNTs. This step is characteristic for the samples treated with nitric acid, and is more evident for the CNT_{ox}-6 sample, indicating the highest population of -OH groups. Finally, at a temperature higher than 500°C, the observed degradation corresponds to the thermal decomposition of the remained disordered carbon. From these results it can be concluded that the best procedure for the oxidation of multi-walled nanotubes implies nitric acid, in agree with literature reports.

4.3. Ruthenium based magnetic nanoparticles carrier

Magnetite nanoparticles are very sensitive to oxygen, and in the presence of air some might undergo oxidation to maghemite (γ-Fe_2O_3) phase. Since both magnetite (Fe_2O_3) and maghemite (γ-Fe_2O_3) have a spinel structure, their diffraction lines are close and it is difficult to distinguish them from one another by X-ray diffraction pattern. Moreover, depending on pH of the aqueous solution containing Fe^{3+} ions, it is also possible to form goethite, α-FeOOH by hydrolysis or by reaction with OH$^-$ species [62]. The formation of hematite (α-Fe_2O_3) is more difficult than that of the maghemite phase, occurring only under thermal dehydration conditions.

To quantify the proportion of iron oxide, formed in a mixture iron oxide-silica, the XRD diffraction patterns were used. As visible in Figure 18, X-ray diffractogram (XRD) of the as synthesized samples showed a diffraction pattern characteristic of dominant magnetite (Fe_3O_4) phase. In particular, the peaks at 2θ equal to 30.1°, 35.4°, 43.1°, 53.4°, 57.1°, and 62.6° can be indexed as

(220), (311), (400), (511), and (440) lattice planes of cubic magnetite, respectively (JCPDS 19-629). Nevertheless, the sharp diffraction lines indicate the presence of trace amounts of goethite phase probably formed as contaminants during the preparation processes. Finally, the broad diffraction line at around $2\theta = 20°$ is due to the amorphous silica shell on the surface of the magnetite nanoparticles. Very important, no characteristic diffraction lines for ruthenium particles appeared after the magnetite impregnation, indicating a well dispersion of these particles on the surface (Figure 27, spectrum in red).
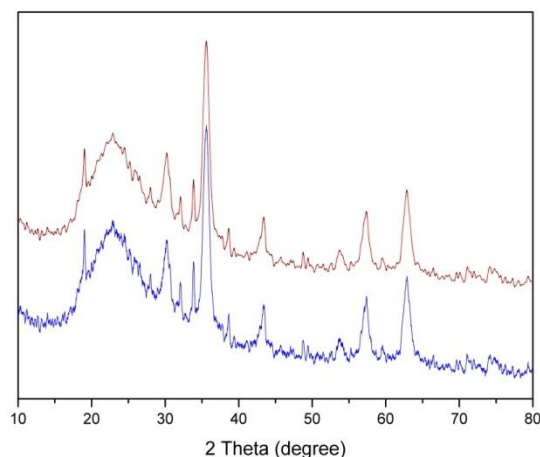

Figure 27. The XRD paterns of Fe_3O_4–SiO_2/NH_2 (blue) and Ru-Fe_3O_4–SiO_2/NH_2 (red) sample

In addition, the crystallite size was calculated through evaluation of the line broadening β and the corresponding Bragg angle θ, by using the Scherrer Equation ($D_{hkl} = 0.9\lambda/\beta\cos\theta$, in which β stands for the half-width of the XRD diffraction line, θ is the peak position in angles, and λ is the CuK$_\alpha$ radiation wavelength, that is 1.54056 Å [63]. The average Fe_3O_4 crystallite size, calculated by applying the Debye-Scherrer equation to the most intense reflection peak (311), was approximately of 18 nm.

The DRIFT spectrum (Figure 28) confirms the coating of the magnetite surface and the existence of amino groups (–NH_2 bending) on the surface of the particles. The presence of magnetite nanoparticles is signalled by the presence of two strong absorption bands at around 632 and 585 cm^{-1}, resulted from the split of v1 band at 570 cm^{-1} corresponding to the Fe–O bond of bulk magnetite (not shown in figure) [64]. The silica network is adsorbed on the magnetite surface by Fe–O–Si bonds which were confirmed by the band at around 584 cm^{-1}. Moreover, the SiO–H and Si–O–Si groups are present in the IR spectra with bands at 1113, 1048 and 989 cm^{-1}. The absorption bands at 922 and 862 cm^{-1} revealed the presence of Si–O–H stretching and OH vibrations on the surface of magnetite, while the two broad bands at 3417 and 1625 cm-1 can be ascribed to the N–H stretching vibration and NH_2

bending mode of free NH$_2$ group, respectively [67]. The presence of the anchored propyl group was confirmed by C–H stretching vibrations that appeared at 2930 and 2862 cm^{-1} while the hydrogen-bonded silanols were confirmed by the bands at around 3200 and 3470 cm^{-1} [65].
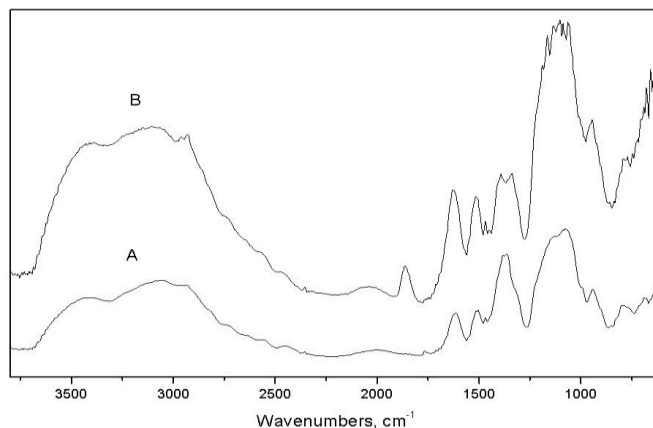

Figure 28. The DRIFT spectra of the Fe$_3$O$_4$–SiO$_2$/NH$_2$ (spectra A) and Ru-Fe$_3$O$_4$–SiO$_2$/NH$_2$ (spectra B) sample

The deposition of ruthenium species led to a reduction of the intensity bands of both 3417 and 1625 cm^{-1} bands, ascribed to the N–H stretching vibration and NH$_2$ bending mode of free NH$_2$ group, in the same time with the appearance of a new band at 1850 cm^{-1} assigned to hydrochloride -C-NH$_3^+$Cl$^-$ species (Figure 19, spectra B). This band confirms the docking of the Ru(OH)$_x$Cl$_{3-x}$ ruthenium species onto the silica-coated magnetite nanoparticles.

Not less important, the obtained catalyst still preserves its magnetic properties, the separation from the aqueous solution being easily done with the aid of an external magnet (Figure 29).

Figure 29. The separation of the Ru-Fe$_3$O$_4$–SiO$_2$/NH$_2$ sample

4.4. Catalytic tests

According to literature [2] the catalytic conversion of lactic acid to alanine takes place through two possible reaction pathways, an indirect (pathway I) and a direct (pathway II) one (Scheme 5, Literature survey). The indirect pathway (I) includes the dehydrogenation of lactic acid to pyruvic acid followed by its reaction with ammonia to afford the 2-iminopropionic acid, which next is hydrogenated to alanine. The direct pathway (II) involves a SN_2 substitution of the α-OH group with an -NH_2 group. In this route the catalyst is crucial in the dehydrogenation step.
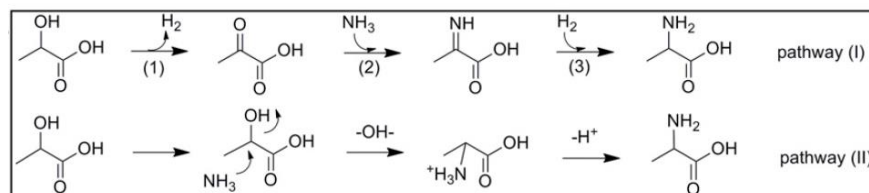
On the other hand, some other authors claim the initial formation of the lactamide intermediate, under the temperature effect, which becomes the raw material for the alanine formation [66] in the presence of the catalyst. Not the last, the formation of the same amide is claimed by other authors [30]. However, in agree with these authors, the alanine is formed by the pathway (I) of dehydrogenation-amination-hydrogenation, paralleling the formation of the lactamide (Figure 30).
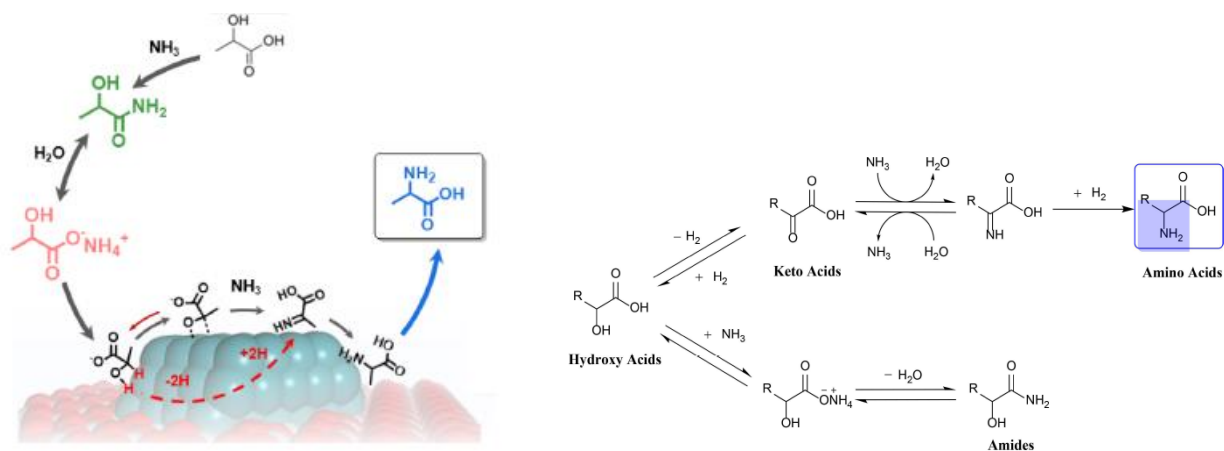

Figure 30. Pathways for the synthesis of alanine from hydroxiacids [30, 66]

In order to confirm the catalytic character of the alanine synthesis the present study started with blank experiments as described in "Experimental section, Catalytic tests". Interesting enough, if in the absence of the ammonia solution lactic acid was not converted in the used reaction conditions, in the

presence of the ammonia solution lactic acid was converted to lactamide, irrespective of the presence or the absence of the hydrogen. The slightly increases of the temperature, from 180 to 200°C, lead to a slightly increases of the lactic acid conversion, from 10.2% to 12.6% with a total selectivity to the observed compound. In agree with Tian et al. [66], lactamide is derived from the neutralization reaction of the lactic acid with ammonia followed by its dehydration to amide under heating conditions. However, in the presence of the Ru-based catalyst, the reaction follows a dehydrogenation-reductive amination pathway. It worth mentioning here that ruthenium has superior catalytic performance over other group VIII metals in the direct amination of hydroxyl group [2, 67]. Moreover, as already stated in literature [30], ruthenium exhibit a high efficiency in the alcohol dehydrogenation which is claimed as the rate-determining step in the amination of lactic acid.

The catalytic system was optimized for the hydrogen pressure (Table 5), the reaction temperature (Table 6), the amount of the catalyst (Table 7) and the reaction time (Table 8) in the presence of 1%Ru/CNT catalyst.

Table 5. The influence of hydrogen pressure upon the lactic acid conversion and alanine selectivity

Entry	Hydrogen pressure (atm)	Conversion (%)	Selectivity (%)		
			Lactamide	Intermediate/by-product	Alanine
1	0	1.6	100	-	-
2	5	3.4	85.0	15.0	-
3	10	31.2	-	56.8	43.2
4	15	42.8	27.9	72.1	-
5	20	71.5	100	-	-

Reaction conditions: 25 mg Ru/CNT(1%), 2.5 mL NH₄OH, 25 μL lactic acid, 200°C, 2 h

As Table 5 shows the conversion of the lactic acid increased with the hydrogen pressure, while at lower hydrogen pressure (5 atm) lactamide was the only formed compound. As the hydrogen pressure is increased from 5 to 10 atm lactamide start to be converted to alanine. However, it is not clearly why a higher hydrogen pressure seems to inhibit the alanine formation. An optimum hydrogen pressure for the alanine synthesis can be explained if we assume the reaction mechanism involves the hydrogenation of an imine intermediate formed through the condensation of ketone with ammonia, in

agree with [30]. In this case a high hydrogen pressure may induce the reverse reaction of ketone hydrogenation, inhibiting the desired amino acid production.

Lactic acid conversion gradually increased when temperature elevated from 180°C to 220°C (Table 6). The catalytic selectivity to the reaction products also showed temperature dependence. Therefore, alanine selectivity initially increased and then, with a further increasing of the temperature, slightly decreased. In contrast, lactamide yield showed opposite trend. These results indicate that the reaction pathway for lactamide formation via neutralization and dehydration was able to happen under a lower temperature. These results also indicate that high reaction temperature may facilitate alcohol dehydrogenation and further transformation to amino acid, underlying the fact that the reaction pathway is the one which involves the imine intermediate. Too high temperature resulted in decreasing the desired product selectivity probably because of alanine decomposition. In conclusion, the optimal temperature choosed for further experiments was 200°C.

Table 6. The influence of reaction temperature upon the lactic acid conversion and alanine selectivity

Entry	Temperature (°C)	Conversion (%)	Selectivity (%)		
			Lactamide	Intermediate/by-product	Alanine
1	180	18.3	100	-	-
2	200	31.2	-	56.8	43.2
3	220	31.4	-	84.3	15.7

Reaction conditions: 25 mg Ru/CNT(1%), 2.5 mL NH$_4$OH, 25 µL lactic acid, 10 atm H$_2$, 2 h

When a low amount of catalyst (5 mg) was used, the lactamide amount was dominant in the reaction products (Table 7). With the increase of catalyst amount, the selectivity in alanine increased and selectivity in lactamide decreased substantially, indicating that the Ru-based catalyst promote the alanine formation. The optimal molar ratio between catalyst and substrate was found to be 100:1 (25 mg catalyst).

Table 7. The influence of amount of catalyst upon the lactic acid conversion and alanine selectivity

Entry	Catalyst (mg)	Conversion (%)	Selectivity (%)		
			Lactamide	Intermediate/by-product	Alanine
1	5	3.87	100	-	-
2	10	6.20	68.3	31.7	-
3	25	31.2	-	56.8	43.2
4	50	37.1	-	55.4	44.6

Reaction conditions: 2.5 mL NH_4OH, 25 μL lactic acid, 10 atm H_2, 200°C, 2 h

Not the last, lactic acid conversion increased with elongated reaction time (Table 8). At the beginning of the reaction, lactamide was obtained as a main product, in line with the blank experiments, in the absence of the catalyst. These results show that lactamide formation is thermodynamically favored and only with the help of a catalyst alanine is formed. However, the alanine passes a maxim in selectivity. This behavior can be an indication of the formation of a by-product which is continuously accumulated alongside the alanine. In Figure 31 the GC analysis and the MS spectrum of alanine is presented.
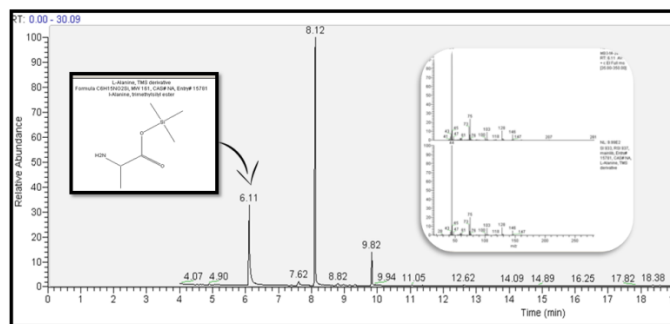

Figure 31. Identification of alanine by GC-MS

Table 8. The influence of reaction time upon the lactic acid conversion and alanine selectivity

Entry	Time (h)	Conversion (%)	Selectivity (%)		
			Lactamide	Intermediate/by-product	Alanine
1	0.5	1.6	100	-	-
2	1	3.19	100	-	-
3	2	31.2	-	56.8	43.2
4	4	42.8	-	85.2	14.8
5	6	71.5	-	88.4	11.6
6	8	72.6	-	100	-

Reaction conditions: 25 mg Ru/CNT(1%), 2.5 mL NH_4OH, 25 mg lactic acid, 10 atm H_2, 200°C

In this stage of the research the pathway of the alanine formation is not very clearly, further experiments being needed to elucidate it. However, based on the obtained results it is possible the catalytic transformation to involves three steps: dehydrogenation of alcohol to ketone (starting from lactamide which loses the ammonia), condensation of the formed ketone with ammonia to imine, which acts like an intermediate and further hydrogenation to the desired product, in agree with the mechanism proposed by Tian et al. [66]. The overall process is represented in Figure 31. The first two steps are reversible reactions [68] and dehydrogenation is rate-determining step for the reported amination of lactic acid.
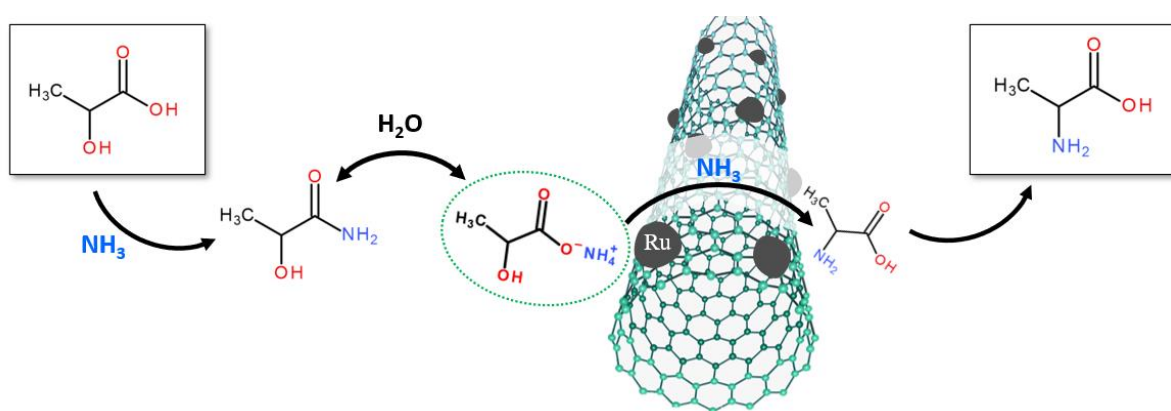

Figure 32. Proposed pathway for converting lactic acid to alanine by amination

The optimum reaction conditions established for the amination of lactic acid into alanine (i.e., 25 mg of catalyst, 10 atm H_2 pressure, 2.5 mL NH_4OH, 2.5 mL H_2O, 25 μL lactic acid, 200°C, 4 h) were used for performing the synthesis in the presence of 3% and 5% Ru/CNT, 1%, 3% and 5% Ru/CNT$_{ox}$-1 and 5%Ru/MNP-SiO$_2$-APTES. The obtained results are presented in the Table 9.

Table 9. The influence of the catalyst type on the lactic acid conversion and alanine selectivity

Entry	Catalyst	Conversion (%)	Selectivity (%)		
			Lactamide	Intermediate	Alanine
1	1%Ru/CNT	42.8	-	85.2	14.8
2	3%Ru/CNT	52.8	-	74.2	25.8
3	5%Ru/CNT	71.5	-	100	-
4	5%Ru/MNP-SiO$_2$-APTES	25.2	-	100	-

Reaction conditions: 25 mg catalyst, 10 atm H_2, 200°C, 2.5 mL NH_4OH, 2.5 mL H_2O 25 μ lactic acid, 4h

It worth noting that in the case of all catalysts the reaction mechanism remains unchanged due to the use of ruthenium which is the key factor in the amination of lactic acid. However, the best loading of ruthenium was 3wt%. Clearly enough the catalytic performance of Ru/CNT can be attributed to the high dispersion of Ru nanoparticles, which was confirmed by STEM measurement. However, it is also not excluded an influence of the reduction degree of the ruthenium nanoparticles.

Conclusions

In summary, we succeeded to synthesize four Ru-based catalysts with CNT and MNP particles as carriers. The characterization of the obtained samples indicate the formation of different kind of ruthenium active phase, as a function of the preparation method and the carrier nature. Therefore, in the case of CNT-based samples, catalysts with ruthenium nanoparticles of different size and oxidation degree were identified on the external side of the CNT tubes: the higher the ruthenium concentration, the larger the nanoparticles; the larger nanoparticles, the higher the proportion of RuO_x (the lower the reduction degree). On the other hand, the MNP-based sample strictly contains cationic ruthenium species with a high degree of dispersion.

CNT carrier was subjected to different oxidation procedures by using different oxidation agents. As characterization results showed, different kind of functional groups (i.e., carboxylic, hydroxyl and epoxy groups) were inserted on the external surface of the CNT, their nature and population highly depending on the applied oxidation procedure. Is not also excluded the formation of $-NH_2$ groups in the case of CNT oxidized with nitric acid. A too aggressive oxidation process, by using mixtures of nitric/sulphuric acids lead to a collapse of the CNT structure through its amorphization.

The preliminary results obtained from the catalytic synthesis of alanine from lactic acid showed that the optimum reaction conditions for the highest selectivity to alanine are: 25 mg catalyst, 2.5 mL NH_4OH, 2.5 mL H_2O, 10 atm H_2, 200°C, 4h. All the catalyst follows the same mechanism which involves three steps: dehydrogenation of alcohol to ketone, condensation of the formed ketone with ammonia to imine, which acts like an intermediate and further hydrogenation to the desired product. The best catalyst was found to be the one which has 3wt% loading of ruthenium.

Acknowledgements

Dissemination

Experimental data obtained in this work were the subject of a communication with the title "Catalytic production of amino acids from biomass-derived intermediates", authors: M. Badea, B. Cojocaru, E. Jacobsen, Vasile I. Parvulescu, Simona M. Coman, accepted to The 13th International Symposium of the Romanian Catalysis Society (RomCat Conference 2022), 22-24 June 2022, Baile Govora, Romania.

References

[1] F.D. Schouwer, L. Claes, A. Vandekerkhove, J. Verduyckt, D. E. De Vos, Protein-rich biomass waste as a resource for future bio-refineries: state of the art, challenges and opportunities, ChemSusChem, 12 (2019) 1272-1303

[2] W. Deng, Y. Wang, S. Zhang, K. M. Gupta, M. J. Hulsey, H. Asakura, L. Liu, Y. Han, E. M. Karp, G. T. Beckham, P. J. Dyson, J. Jiang, T. Tanaka, Y. Wang, Catalytic amino acid production from biomass derived intermediates, PNAS, 115 (2018) 5093-5098

[3] P. Serp, M. Corrias, P. Kalck, Carbon nanotubes and nanofibers in catalysis, Appl. Catal. A: General, 253 (2003) 337-358

[4] Z. Zhong, B. Liu, L. Sun, J. Ding, J. Lin, K.L. Tan, Dispersing and coating of transition metals Co, Fe and Ni on carbon materials, Chem. Phys. Lett., 362 (2002) 135-143

[5] P. Chen, X. Wu, J. Lin, K.L. Tan, Synthesis of Cu Nanoparticles and Microsized Fibers by Using Carbon Nanotubes as a Template, J. Phys. Chem, 103, 22 (1999) 4559-4561

[6] A. Kuznetsova, I. Popova, J.T. Yates, M.J. Bronikowski, C.B. Huffman, J. Liu, R.E. Smalley, H.H. Hwu, J.G. Chen, Oxygen-Containing Functional Groups on Single-Wall Carbon Nanotubes: NEXAFS and Vibrational Spectroscopic Studies, J. Am. Chem. Soc. , 123 (2001) 10699-10704

[7] R. Giordano, P. Serp, P. Kalck, Y. Kihn, J. Schreiber, C. Marhic, J.L. Duvail, Preparation of Rhodium Catalysts Supported on Carbon Nanotubes by a Surface Mediated Organometallic Reaction, Eur. J. Inog. Chem., 2003, 610-617

[8] S. Shylesh, V. Schunermann, W.R. Thiel, Magnetically Separable Nanocatalysts: Bridges between Homogeneous and Heterogeneous Catalysis, Angew. Chem. Int. Ed., 49 (2010) 3428-3459

[9] E. McCafferty, J.P. Wightman, Determination of the Concentration of Surface hydroxyl Groups on Metal Oxide Films by a Quantitative XPS Method, Surf. Interface Anal. 26 (1998) 549-564

[10] I. Podolean, V. Kuncser, N. Gheorghe, D. Macovei, V.I. Parvulescu, S.M. Coman, Ru-based magnetic nanoparticles (MNP) for succinic acid synthesis from levulinic acid, Green Chem., 15 (2013) 3077-3082

[11] P. Sudarsanam, R. Zhong, S. Van den Bosch, S. M. Coman, V. I. Parvulescu, B. F. Sels, Functionalised heterogeneous catalysts for sustainable biomass valorisation, Chem. Soc. Rev., 47 (2018) 8349-8402

[12] C. H. Zhou, X. Xia, C. X. Lin, D. S. Tong, J. Beltramini, Catalytic conversion of lignocellulosic biomass to fine chemicals and fuels, Chem. Soc. Rev., 40 (2011) 5588-5617

[13] J. A. Geboers, S. Van de Vyver, R. Ooms, B. Op de Beeck, P. A. Jacobs, B. F. Sels, Chemocatalytic conversion of cellulose: opportunities, advances and pitfalls, Catal. Sci. Technol., 1 (2011) 714-726

[14] R. Abejón, A bibliometric Study of Scientific Publications regarding Hemicellulose Valorization during the 2000-2016 Period: Identification of Alternatives and Hot Topics, Chem.Eng., 2 (2018) 1-31

[15] S. M. Coman, M. Tudorache, V. I. Parvulescu, An Introduction to Green Chemistry, Future Science, 2013, Chapter 4: Green catalysis methods: catalysis for lignocellulosic biomass capitalization, 54-69

[16] R. Rinaldi, F. Schüth, Design of solid catalysts for the conversion of biomass, Energy. Environ. Sci., 2 (2009) 610-626

[17] Y. Wang, S. Furukawa, S. Song, Q. He, H. Asakura, N. Yan, Catalytic production of alanine from waste glycerol, Angew. Chem. Int. Ed., 59 (2020) 2289-2293

[18] M. Dusselier, P. V. Wouwe, A. Dewaele, E. Makshina, B. F. Sels, Lactic acid as a platform chemical in the biobased economy: the role of chemocatalysis, Energy Environ. Sci, 6 (2013) 1415-1442

[19] G. G. Millán, S. Hellsten, J. Llorca, R. Luque, H. Sixta, A. M. Balu, Recent Asvances in the Catalytic Production of Platform Chemical from Holocellulosic Biomass, ChemCatChem, 11 (2019) 1-22

[20] M. Janssen, Market potential of biorefinery products, Publications. Lib. Chalmers. Se., 2012 , 1-10

[21] M. D'Este, M. Alvarado-Morales, I. Angelidaki, Amino acids production focusing on fermentation technology – A review, Biotechnol. Adv., 36 (2018) 14-25

[22] E. Scott, F. Peter, J. Sanders, Biomass in the manufacture of industrial products – the use of proteins and amino acids, Appl. Microbiol. Biotechnol., 75 (2007) 751-762

[23] S. L. Miller, A Producion of Amino Acids Under Possible Primitive Earth Conditions, Science, 117 (1953) 528-29

[24] K. Harada, Asymmetric Synthesis of α-Amino-acids by the Strecker Synthesis, Nature, 4912 (1963) 1201

[25] U. D. Wermuth, I. D. Jenkins, R. C. Bott, K. A. Byriel, G. Smith, Some Stereochemical Aspects of the Strecker Synthesis and the Bucherer-Bergs Reaction, Aust. J. Chem., 57 (2004) 461-465

[26] M. S. Gibson, R. W. Bradshaw, The Gabriel Synthesis of Primary Amines, Angew. Chem. 7 (1968) 919-929

[27] A. Behr, T. Seidensticker, Chemistry of Renewables : An introduction, Springer, 2020, Chapter 14: Building Blocks of Life – Amino Acids, 251-263

[28] S. Song, J. Qu, P. Han, M. J. Hulsey, G. Zhang, Y. Wang, S. Wang, D. Chen, J. Lu, N. Yan, Visible-light-driven amino acids production from biomass-based feedstocks over ultrathin CdS nanosheets, Nat. Commun., 4899 (2020) 1-10

[29] T. Fukushima, M. Yamauchi, Electrosynthesis of amino acids from biomass-derivable acids on titanium dioxide, Chem. Comm., 55 (2019) 12721-12724

[30] Z. Xie, B. Chen, F. Peng, M. Liu, H. Liu, G. Yang, B. Han, Highly Efficient Synthesis of Amino Acids by Amination of Bio-derived Hydroxy Acids with Ammonia over Ru Supported on N-doped Carbon Nanotube, ChemSusChem, 13 (2020) 5683-5689

[31] A. Negoi, I.T. Trotus, O.M. Steiner, M. Tudorache, V. Kuncser, D. Macovei, V.I. Parvulescu, S.M. Coman, Direct Synthesis of Sorbitol and Glycerol from Cellulose over Ionic Ru/Magnetite Nanoparticles in the Absence of External Hydrogen, ChemSusChem, 6 (2013) 2090-2094

[32] S.J. Greeg, K.S. Sing, Adsorption, Surface Area and Porosity, 1982, 957

[33] Q.H. Yang, P.X. Hou, S. Bai, M.Z. Wang, H.M. Cheng, Adsorption and capillarity of nitrogen in aggregated multi-walled carbon nanotubes, Chem. Phys. Lett., 345 (2001) 18-24

[34] M. Ran, Y. Liu, W. Chu, A. Borgna, Enhanced Conversion of Cellobiose to Sugar Alcohols by Controlled Dispersion of Ruthenium Nanoparticles Inside Carbon Nanotube Channels, Catal. Let, 143 (2013) 1139-1144

[35] J. Kang, W. Deng, Q. Zhang, Y. Wang, Ru particle size effect in Ru/CNT-catalyzed Fischer-Tropsch synthesis, J. Energy Chem., 22 (2013) 321-328

[36] S. Thoka, C.M. Tsai, Z. Tong, A. Jena, F.M. Wang, C.C. Hsu, H. Chang, S.F. Hu, R.S. Liu, Comparative Study of Li-CO_2 and Na-CO_2 Batteries with Ru@CNT as a Cathode Catalyst, ACS Appl. Mater. Interfaces, 13 (2021) 480-490

[37] F. Su, L. Lv, F.Y. Lee, T. Liu, A.I. Cooper, X.S. Zhao, Thermally Reduced Ruthenium Nanoparticles as a Highly Active Heterogeneous Catalyst for Hydrogenation of Monoaromatics, J. Am. Chem. Soc., 129 (2007) 14213-14223

[38] Q. Zhang, L. Gao, J. Guo, Effects of calcination on the photocatalytic properties of nanosized TiO_2 powders prepared by $TiCl_4$ hydrolysis, Appl. Catal. B: Environ., 26 (2000) 207-215

[39] W. Chen, Z. Fan, X. Pan, X. Bao, Effect of Confinement in Carbon Nanotubes on the Activity of Fisher-Tropsch Iron Catalyst, J. Am. Chem. Soc., 130 (2008) 9414-9419

[40] R.M.M. Abbaslou, A. Tavassoli, J. Soltan, A.K. Dalai, Iron catalyst supported on carbon nanotubes for Fischer-Tropsch synthesis: Effect of catalytic site position, Appl. Catal. A: Gen., 367 (2009) 47-52

[41] F. Lonyi, J. Valyon, On the interpretation of the NH_3-TPD patters of H-ZSM-5 and H-mordenite, Micropor. Mesopor. Mat., 47 (2001) 293-301

[42] N.R. Meshram, S.G. Hedge, S.B. Kulkarni, Active sites on ZSM-5 zeolites for toluene disproportionation, Zeolites, 6 (1986) 434-438

[43] H. Igi, N. Katana, M. Niwa, in: M. M. J. Treacy, B. K. Marcus, M. E. Bisher, J. B. Higgins (Eds.), Proceedings of the 12th International Zeolite Conference, Materials Research Society, Warrendale, PA, 1999, 2643

[44] C.F. Wang, X.L. Pan, X.H. Bao, Direct production of light olefins from syngas over a carbon nanotube confined iron catalyst, Chem. Phys. Lett., 55 (2010) 1117-1119

[45] J.T. Miller, B.L. Meyers, F.S. Modica, G.S. Lane, M. Vaarkamp, D.C. Koningsberger, Hydrogen Temperature-Programmed Desorption (H_2 TPD) of Supported Platinum Catalysts, J. Catal., 143 (1993) 395-408

[46] G. Vidali, Potentials of physical adsorption, Surf. Sci. Reports, 12 (1991) 133-181

[47] K. Masenelli-Varlot, E. McRae, N. Dupont-Pavlovsky, Comparative adsorption of simple molecules on carbon nanotubes. Dependence of the adsorption properties on the nanotube morphology, Appl. Surf. Sci., 196 (2002) 209-215

[48] T. Szilagyi, Fourier-Transform Infrared Study of Weak Adsorption of hydrogen on Pt/SiO_2, J. Catal., 121 (1990) 223-227

[49] J. Chen, M.A. Hamon, H. Hu, Y. Chen, A.M. Rao, P.C. Eklund, R.C. Haddon, Solution Properties of Single-Walled Carbon Nanotubes, Science, 282 (1998) 95-98

[50] M.E. Lipinska, S.L.H. Rebelo, M.F.R. Pereira, J.A.N.F. Gomes, C. Freire, J.L. Figueiredo, New insights into the functionalization of multi-walled carbon nanotubes with aniline derivatives, Carbon, 50 (2012) 3280-3294

[51] N. Yao, V. Lordi, S.X.C. Ma, Structure and oxidation patterns of carbon nanotubes, J. Mater. Res, 13, 9 (1998) 2432-2437

[52] B.C. Satishkumar, A. Govinndaraj, J. Mofokeng, G.N. Subbanna, C.N.R. Rao, Novel experiments with carbon nanotubes: opening, filling, closing and functionalizing nanotubes, J. Phys. B: At. Mol. Opt. Phys, 29 (1996) 4925-4934

[53] S. Aftab, S.T. Hussain, M. Siddique, H. Nawaz, Comprehensive study of trends in the functionalization of CNTs using same oxidizing acids in different conditions, Der. Pharma. Chemica, 2 (2010) 354-365

[54] C.P. Poole, F.J. Owens, Introduction in Nanotechnology, Wiley, 2003, Chapter 5.4: Carbon Nanotubes, 114-124

[55] G.W. Lee, J. Kim, J. Yoon, J.S. Bae, B.C. Shin, I.S. Kim, W. Oh, M. Ree, Structural characterization of carboxylated multi-walled carbon nanotubes, Thin Solid Films, 516 (2008) 5781-5784

[56] M.L. Toebes. J.M.P. van Heeswijk, J.H. Bitter, A. Jos van Dillen. K.P. de Jong, The influence of oxidation on the texture and the number of oxygen-containing surface groups of carbon nanofibers, Carbon, 42 (2004) 307-315

[57] G.S. Szymanski, T. Grzybek, H. Papp, Influence of nitrogen surface functionalities on the catalytic activity of activated carbon in low temperature SCR of NO_x with NH_3, Catal., 90 (2004) 51-59

[58] J. Zhang, H. Zou, Q. Qing, Y. Yang, Q. Li, Z. Liu, X. Guo, Z. Du, Effect of Chemical Oxidation on the Structure of Single-Walled Carbon Nanotubes, J. Phys. Chem. B, 107 (2003) 3712-3718

[59] M.R. loos, L.A.F. Coelho, S.H. Pezzin, S.C. Amico, Effect of Carbon Nanotubes Addition on the Mechanical and Thermal Properties of Epoxy Matrices, Mater. Res., 11 (2008) 347-352

[60] V. Datsyuk, M. Kalyva, K. Papagelis, J. Pathenios, D. Tasis, A. Siokou, I. Kallitsis, C. Galiotis, Chemical oxidation of multiwalled carbon nanotubes, Carbon, 46 (2008) 833-840

[61] S.A. Chernyak, A.S. Ivanov, K.I. Maslakov, A.V. Egorov, Z. Shen, S.S. Savilov, V.V. Lunin, Oxidation, defunctionalisation and catalyst life cycle of carbon nanotubes: a Raman spectroscopy view, Phys. Chem. Chem. Phys, 19 (2017), 2276-2285

[62] M. Yamaura, R.L. Camilo, L.C. Sampaio, M.A. Macedo, M. Nakamura, H.E. Toma, Preparation and characterization of (3-aminopropyl) triethoxysilane-coated magnetite nanoparticles, J. Magn. Magn. Mater., 279 (2004) 210-217

[63] M.P. Morales, S.V. Verdaguer, M.I. Montero, C.J. Serna, Surface and Internal Spin Canting in γ-Fe_2O_3 Nanoparticles, Chem. Mater, 11 (1999) 3058-3064

[64] M. Ma, Y. Zhang, W. Yu, H. Shen, H. Zhang, N. Gu, Preparation and characterization of magnetite nanoparticles coated by amino silane, Colloids and Surfaces A: Physicochem. Eng. Aspects, 212 (2003) 219-226

[65] L.D. White, C.P. Tripp, Reaction of (3-aminopropyl)dimethylethoxyxilane with Amine Catalysts on Silica Surfaces, J. Colloid Interface Sci., 232 (2000) 400-407

[66] S. Tian, Y. Jiao, Z. Gao, Y. Xu, L. Fu, H, Fu, W. Zhou, C. Hu, G. Liu, M. Wang, D. Ma, Catalytic Amination of Polylactic acid to Alanine, J. Am. Chem. Soc., 143 (2021) 16358-16363

[67] D. Ruiz, A. Aho, T. Saloranta, K. Eranen, J. Warna, R. Leino, D. Y. Murzin, Direct amination of dodecanol with NH_3 over heterogeneous catalysts. Catalyst screening and kinetic modelling, Chem. Eng. J., 307 (2017) 739-749

[68] D. Pingen, C. Muller, D. Vogt, Direct Amination of Secondary Alcohols Using Ammonia, Angew. Chem. Int. Ed., 49 (2010) 8130-8133

Annex 1. Thermogravimetric analysis of CNT carrier

In order to establish the optimum temperature for the calcination of samples 1%Ru/CNT, 3%Ru/CNT and 5%Ru/CNT the TG analysis of CNT was previously performed. According to the TGA profile in the air atmosphere (Figure 1), the mass loss of the CNT starts slowly in the temperature range 440-460 °C. However, after 500°C the CNT begins to be fast oxidized (a process possible catalysed by the transition metals remained into the material from the synthesis of CNT) and the mass of the sample quickly declines with the increase of temperature. Bearing in mind this, the calcination step of the Ru-based catalysts was performed at 350°C in order to avoid the decomposition of the support.
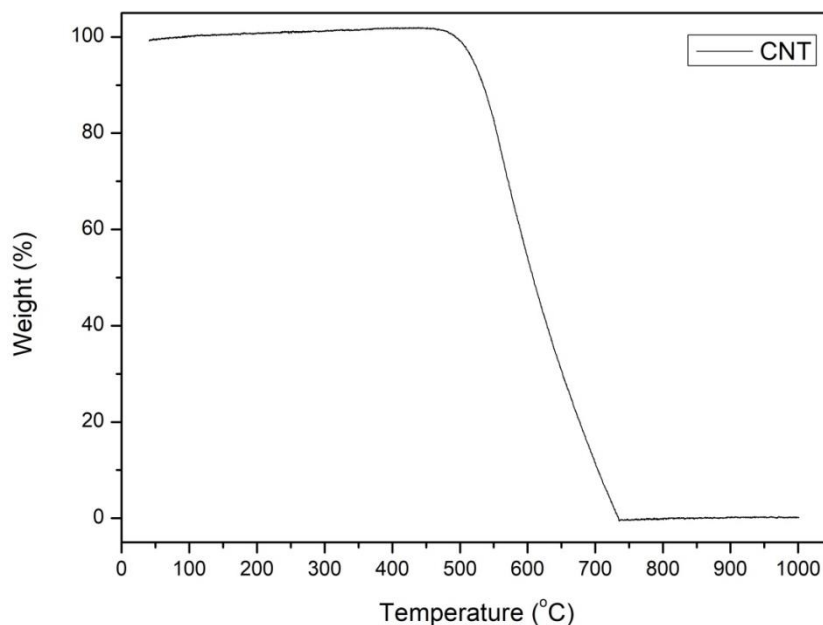

Figure 1. TGA profile in air atmosphere for as-received CNT

Annex 2. Detailed oxidation procedures for the synthesis of CNT$_{ox}$ samples.

CNT$_{ox}$-1: 2 g of the agglomerated MWCNTSs were dispersed in 200 mL nitric acid (65 wt%) in a 500 mL round bottom flask. In order to minimize the tubes damage, a low power sonicating bath and a relatively low acid exposure time were used. Therefore, the mixture was sonicated in a conventional ultrasonic bath for 3 h, promoting CNT disentanglement within the acid solution. In order to neutralize the strong acidity NaOH solution was added in the slurry. Then, the slurry was filtered and thoroughly washed with distilled water, until a neutral pH. Finally, the slurry was filtered using PTFE membrane filter with 0.45 μm pore sized and then dried at 80°C for 24 h.

CNT$_{ox}$-2: 1 g of MWCNTs were dispersed in 200 mL nitric acid (65 wt%) in a 500 mL round bottom flask. The mixture was sonicated for 3 h, promoting carbon nanotubes disentanglement within the acid solution. Next, the reaction flask equipped with reflux condenser, magnetic stirred and thermometer was mounted in the preheated oil bath and the mixture was refluxed for 1 h at 80°C and another hour at 100°C. After cooling at r.t., to the resulted slurry water was added and then filtered. The resulted solid was washed up to neutral pH and dried at 80°C for 24 h.

CNT$_{ox}$-3: 1 g of MWCNTs were dispersed in 200 mL of fresh nitric acid (65 wt%) in a 500 mL round bottom flask. The mixture was sonicated for 3 h in order to promote the disentanglement of CNTs within the acid solution. Next, the round bottom flask equipped with reflux condenser, magnetic stirring and thermometer was mounted in the preheated oil bath. The mixture was refluxed for 2 h at 80°C. After cooling at r.t., to the resulted slurry water was added and then filtered. The resulted solid was washed up to neutral pH and dried at 80°C for 24 h.

CNT$_{ox}$-4: 0.3 g of the agglomerated MWCNTs were mixed with 70 mL mixture of HNO$_3$ (65 wt%) and H$_2$SO$_4$ 8M by mechanically stirring on a hot plate, for 15 min at 60°C and then sonicated for 2 h. Then, the slurry was filtered and thoroughly washed with distilled water, until a neutral pH. The resulted solid was dried at 80°C for 24 h.

CNT$_{ox}$-5: 0.3 g of the agglomerated MWCNTs were mixed with 70 mL mixture of HNO$_3$ (65 wt%) and H$_2$SO$_4$ 3M by mechanically stirring on a hot plate for 15 min at 60°C, and then sonicated for 2 h. The solid was separated, washed with distilled water, re-immnersed in H$_2$O$_2$ (30% v/v) and the

procedure was identically repeated. Then, the slurry was thoroughly washed with distilled water, until a neutral pH and filtered. The resulted solid was dried at 80°C for 24 h.

CNT$_{ox}$-6: 0.3 g of the agglomerated MWCNTs were mixed with 7.5 mL mixture of HNO$_3$ (65 wt%) by mechanically stirring in a hot plate for 15 min at 60°C, and sonicated for 3 h. The solid was separated, washed with distilled water, re-immersed in H$_2$O$_2$ (30% v/v) and the procedure was identically repeated. The subsequent treatment with H$_2$O$_2$ was given in order to complete the oxidative process started by nitric acid, but in a gentler manner. Then, the slurry was thoroughly washed with distilled water, until a neutral pH and filtered. The resulted solid was dried at 80°C for 24 h.

CNT$_{ox}$-7: 0.1 g of the agglomerated CNTs were mixed with 5 mL hydrogen peroxide (30%) by mechanically stirring in a hot plate at 65°C for 72h. 2.5 mL of hydrogen peroxide was added at each 24h in order to keep a constant volume. After oxidizing the nanotubes the slurry was thoroughly washed with distilled water until a neutral pH and filtered. The resulting solid was dried at 80°C for 24 h.

CNT$_{ox}$-8: 0.1 g of the agglomerated CNTs were dispersed in 10 mL nitric acid (65 wt%) in a 50 mL round bottom flask. The mixture was sonicated for 3 h in a conventional ultrasonic bath Bandelin SONOREX™ SUPER with build-in heating, RK 103H, promoting CNT disentanglement within the acid solution. Then, the slurry was filtered and thoroughly washed with distilled water until a neutral pH. Recovered filter was immersed into distillated water and ultrasonated until the carbon nanotubes redispersion (2 min). The redispersed carbon nanotubes were then centrifuged for 5 min at 4000 rpm. Remained nanotubes into the liquid phase were collected by adding 100 mL dichloromethane (CH$_2$Cl$_2$) followed by filtration, whishing with additional amounts of CH$_2$Cl$_2$ and ultrasonication for 3h. The obtained solution was the subject of a slow evaporation (r.t. for 24 h). Finally, the obtained solid was completely dried at 80°C for 24 h.

13TH INTERNATIONAL SYMPOSIUM OF THE ROMANIAN CATALYSIS SOCIETY

THIS CERTIFIES THAT PhD Stud.

Matica Alexandra Badea

University of Bucharest

attended the RomCat2022 conference which was held in
Băile Govora, Romania on June 22-24, 2022

President of the Romanian Catalysis Society

Prof. Vasile Parvulescu

§ SOCIETATEA
C DE CATALIZA
R DIN ROMANIA

RomCat
22-24 June 2022
Băile-Govora, Romania

Norwegian University of Science and Technology

N-7491 Trondheim, Norway
Telephone: +47 73596256
E-mail: Elisabeth.E.Jacobsen@ntnu.no   *Department of Chemistry*

Trondheim, June 12th 2022

To whom it may concern

I hereby confirm that master candidate Mara Badea, University of Bucharest, Romania, can use the analysis results of her Ruthenium Carbon Nanotube (RuCNT) catalyst samples performed by Scanning Transmission Electron Microscopy (STEM) at NTNU Nanolab.

The analyses were performed during her Short Term Scientific Mission stay at Department of Chemistry, Norwegian University of Science and Technology, under my supervision, during September 1-30- 2021.

Best regards,

Elisabeth E Jacobsen

Elisabeth E. Jacobsen
Associate professor, PhD